Lagrangian tracking methods applied to free surface boundaries in numerical geodynamic models

Timothy Gray[1], Paul J. Tackley[1], and TarasV. Gerya[1]

[1]Institute of Geophysics, Department of Earth and Planetary Sciences, ETH Zürich, Sonneggstrasse 5, 8092 Zurich, Switzerland

Correspondence: Timothy Gray (timothy.gray@eaps.ethz.ch)

Abstract. A desirable characteristic of mantle convection models is the ability to determine surface topography evolution over time on a global scale. This capability is increasingly important due to growing interest in coupling planetary geodynamics with climate, landscape, habitats, and biological evolution systems. A common way of achieving this in numerical geodynamic models with a fixed Eulerian grid is through the implementation of a free-surface boundary condition using the sticky air method in conjunction with an appropriate method of tracking the free surface. Although existing methods for tracking the interface between the air and rock layers are available, they often struggle to provide high-resolution results on a global scale without incurring significant computational costs. We propose a method for representing surfaces directly using Lagrangian markers that can track the location of a free surface in 2D and 3D models and test it using the finite-volume mantle convection code StagYY. This approach offers a direct, high-resolution representation of the surface without the need for a large number of high-cost ~~tracers~~ volumetric markers throughout the model domain. Benchmarks demonstrate the effectiveness of this method compared to the commonly-used marker-in-cell method. The direct representation of the surface enables additional features such as the direct tracking of sea levels over time, potential for coupling with surface process models on the global scale, and enables the implementation of alternative discretisations of the Stokes equations to improve Stokes solver accuracy near the free surface boundary.

1 Introduction

Modelling the evolution of planetary surfaces over time has attracted considerable attention in geodynamics, since surface topography is a primary observable of a planet's internal dynamics and can also change the dynamics compared to assuming a flat surface (e.g. Crameri et al. (2012b)). The growing interest in coupled planetary systems, particularly the coupling between geodynamic processes, climatic processes, and biological evolution, further motivates the study of topographic evolution due to the coupling between these systems occurring primarily at the surface. The study of these couplings, also referred to as *biogeodynamics* (Zerkle, 2018; Stern and Gerya, 2023), requires accurate methods of determining how mantle convection affects the surface, and in turn affects other systems in order to study fundamental questions regarding the habitability of planetary bodies.

Geodynamic models commonly represent a free surface using a fixed, Eulerian grid with ~~"sticky air"~~ "sticky air", a low-viscosity, low-density layer above the surface that approximates a true free surface boundary condition, representing material above the surface (e.g. the various modelling codes in Crameri et al. (2012a) and Schmeling et al. (2008)). Modelling free surfaces on fixed Eulerian grids ~~in numerical geodynamic models~~ requires two key components: an appropriate solver that can model or approximate the solution to the Stokes equation with a free surface boundary condition, and a method of tracking the location of the surface over time.

This study implements a method for tracking free surfaces on a global scale ~~. The method is implemented into~~ in StagYY (Tackley, 2008), which uses the staggered-grid finite difference discretisation ~~(equivalent to the finite volume discretisation), as is often used~~ as is common in geodynamic modelling codes (e.g. (Patankar, 1980; Ogawa et al., 1991; Tackley, 1993; Trompert and Hansen, 1996; Gerya and Yuen, 2007; Tackley, 2008; Gerya et al., 2015; Kaus et al., 2016))~~due to its simplicity in discretising the governing equations and compatibility with efficient multigrid solvers in both 2D and 3D. However, the~~ . The free surface tracking methods presented are also generally applicable to other Eulerian-grid geodynamic codes.

~~For clarity, the Lagrangian points already implemented in StagYY and distributed throughout the model domain are hereafter referred to as "tracers". The existing surface tracking approach—the marker-in-cell technique —uses these tracers to infer the surface location. In contrast, Lagrangian points introduced in this study specifically for tracking the free surface are referred to as "surface markers".~~

~~In StagYY, as in~~ The standard technique for interface tracking in StagYY and many other codes ~~, the standard technique for interface tracking employs Lagrangian tracers using a~~ is the marker-in-cell method~~. In this approach, Lagrangian tracers~~ , in which Lagrangian markers distributed throughout the model ~~are used to represent information about material properties (in this case whether they are~~ domain carry material type information (rock or air), which ~~are then averaged to determine the~~ is averaged onto the grid to determine density and viscosity fields ~~used by the Stokes solver, as well as the location of the free surface. However, when running large-scale global models, particularly in 3D, computational cells are typically large due to computational limitations. A typical global scale~~ and infer the surface location (Tackley and King, 2003). Two averaging approaches are common: simple cell (boxcar) averaging, and the more accurate linear shape function averaging used as the default in StagYY, which additionally weights markers by their position within the cell. While effective, both approaches share a fundamental limitation: surface quality depends strongly on the number of markers per cell (here referred to as marker density). For a global-scale 3D ~~spherical model can only achieve a~~ model with a typical vertical resolution of ~~approximately~~ $\approx$10 km ~~near the surface while remaining computationally tractable, even after refining the vertical grid spacing near the surface (Coltice et al., 2019). For modelling topography on Earth-like planets, where the maximum topographic variations are on the order of $\pm$10 km , this vertical cellresolution necessitates a method for tracking topography on a fine sub-grid scale. Using the marker-in-cell method, finer resolution can be achieved trivially by increasing the number of tracers. However, this approach scales poorly: doubling the vertical tracer~~ (Coltice et al., 2019), resolving topographic variations of order $\pm$10 km at 100 m sensitivity would require at least 100 markers per cell. Achieving this is computationally prohibitive: marker advection cost scales linearly with marker density, and in practice dominates total runtime at the densities required for accurate surface tracking, accounting for up to 77% of total runtime at 500 markers per cell in our tests. Doubling vertical marker density

requires 4~~times as many tracers~~ × more markers in 2D and 8~~times as many~~ × more in 3D~~. This increases both memory usage and computational costs for storing and advecting these tracers. This inefficiency motivates alternative methods of~~ , making this approach impractical at global scale.

For clarity, the Lagrangian points already implemented in StagYY are hereafter referred to as "markers", while Lagrangian points introduced in this study specifically for tracking the free surface are referred to as "surface markers".

A successful surface tracking method must ~~satisfy several criteria:~~

~~Provide~~ provide fine sub-grid resolution of topography on the global scale~~. Remain~~ , remain stable over many timesteps and across diverse geodynamic regimes ~~, including subduction. Ensure~~ including subduction, ensure compatibility with the underlying Stokes solver~~(e.g. preserve mass conservation). Reduce~~ , and reduce computational cost relative to the marker-in-cell method.

Interface-tracking approaches ~~that meet~~ meeting these criteria include level-set and volume-of-fluid methods. However, one of the conceptually simplest options is to track interfaces directly using Lagrangian markers~~— often~~ , referred to as direct interface tracking in the CFD literature (Tezduyar, 2006)~~. In this approach,~~ , in which the surface is explicitly represented by ~~Lagrangian~~ markers that follow the surface flow. ~~Using such markers only at the surface~~ Confining markers to the surface alone avoids the scaling limitations of the full marker-in-cell approach~~, offering potentially higher accuracy at lower computational cost~~.

Several characteristics of ~~surfaces in global scale geodynamics make Lagrangian interface tracking attractive:~~

planetary surfaces make this approach particularly attractive. For Earth-like planets, the maximum surface deviation (~~±10~~ ±10 km) is ~~relatively~~ small relative to ~~the mantle's total~~ total mantle thickness (2,890 km)~~. The~~ , and the surface height can be ~~considered a one-to-one~~ treated as a single-valued function of position~~(i.e. the surface cannot overlap itself).~~ . Planetary surfaces are sharp interfaces ~~; there is no diffused mixed regionof air and rock in the vicinity of the surface.~~ with no diffuse mixed region. Many geodynamic codes ~~, including StagYY,~~ already use Lagrangian ~~tracers, enabling simple implementation through the repurposing of existing code. Lagrangian markers can provide fine sub-grid level resolution, essential for the global scale where the Eulerian mesh is coarse.~~ markers, enabling straightforward implementation by adapting existing routines. The number of ~~markers required to track the surface is generally small in comparison~~ surface markers required is small compared to the total ~~number of markers used for other purposes throughout the mantle. Lagrangian~~ marker population, and surface markers are well-suited for parallelisation ~~,~~including on GPUs.

In this study, we implement Lagrangian interface tracking in StagYY and introduce two methods: the *bilinear method* and the *integral method*, which differ in how they transfer surface information to the underlying grid. We assess their computational performance and ~~their ability to track~~ accuracy in tracking a free-surface boundary condition, comparing them with the existing marker-in-cell approach.

2 Limitations of the marker-in-cell method

1.1 General approach

The marker-in-cell method is the approach used to track free surfaces in StagYY and many other geodynamic codes. Lagrangian tracers throughout the model domain track material type (rock or air in the examples here; often many other quantities). To obtain the position of the surface, the tracer distribution is first turned into a compositional field representing air fraction, then the vertical location of the surface is inferred from this air fraction field. Air fraction is calculated as ratio of the number of air tracers to total (rock+air) tracers in a cell, with the numbers of tracers being calculating using one of two sampling (shape) functions, as in Tackley and King (2003).

1.0.1 Cell averaging/boxcar averaging

The simplest method of determining the location of the free surface is by first computing a compositional field C by averaging numbers of tracers of each type per cell (Figure **??**). A cell containing only rock tracers will have $C_{\text{rock}} = 1$ and $C_{\text{air}} = 0$, a cell containing only air tracers will have $C_{\text{rock}} = 0$ and $C_{\text{air}} = 1$, while a cell containing the surface will have both Cs between 0 and 1. The surface location is then derived from this boxcar averaged field.

While this method enables vertical sub-grid level topographic resolution, doing so accurately requires large numbers of tracers per cell. For example, providing 100 m topography sensitivity on a grid with a vertical resolution of 10 km would require at least 100 tracers per cell. Random noise inherent in the tracers also hinders the ability of this method to accurately track surfaces. As a tracer moved from one cell to another, the composition of both cells changes discontinuously.

1.0.1 Linear shape function averaging

It is possible to overcome some of the limitations of the simple cell averaging method by additionally taking into account the positions of the tracers. This is done by using linear shape function averaging, where the compositional field C is determined for a given cell by weighted averaging of tracers, with this weighting function being linear and centred at the cell centre, resulting in a triangular shape (Figure **??**), similar to linear shape functions in the finite element method. By weighting the markers, information about the position of the tracers is also taken into account. Determining the surface location when using this method then requires the solution of a geometrical problem relating to the triangular shape of the shape function, which causes two cells vertically to have C_{air} between 0 and 1. As this is much more accurate than the cell averaging approach, linear shape function averaging is the default surface tracking method used by StagYY and thus what is used in the presented tests.

There are two averaging methods used in determining the surface location from a tracer field (illustrated in 1D): boxcar averaging (or cell averaging), and linear shape function averaging. With boxcar averaging, a simple count of rock and air tracers (blue and red) in a given cell is performed, and the location of the surface inferred from C_i. With linear shape function averaging, a weighting function is first applied which includes information on both number and location of tracers in a cell.

Although an improvement on the simple cell averaging approach, linear shape function averaging retains a dependence on number of tracers per cell, which can result in poor performance when modelling small variations in topography.

1.1 Testing the limitations of the marker-in-cell method

To quantify tracer density–dependent noise in the existing method (where tracer density here means the number of tracers per cell), we use a simple dimensionless 3D Cartesian StagYY model (Figure 20). The viscosity is constant and set to a nondimensional value of $\eta = 1$, convecting with a Rayleigh number of 10^7. Surface topography is expressed as a fraction of the normalised mantle thickness (set to 1). Temperature is also nondimensionalised, ranging from $T = 0$ at the surface to $T = 1$ at the core-mantle boundary. To better illustrate the effect of tracer density, a relatively coarse resolution of 64x64x32 using uniform cubic cells and no surface mesh refinement. Large surface cells highlight the need for sub-grid resolution to capture topography accurately.

A nondimensional constant-viscosity model ($\mathrm{Ra} = 10^7$) in 3D Cartesian geometry is used to investigate the dependence of the quality of surface topography reconstruction on tracer density (Figure **??**). Topography is tracked with tracers using the marker-in-cell method, and a sticky air discretisation with a viscosity contrast of $\eta_{\mathrm{air}}/\eta_{\mathrm{rock}} = 10^{-3}$ is used. A relatively coarse resolution of 64x64x32 is used to better highlight the effect of low marker densities on topography.

After 5,000 time steps, the simple models have reached statistically steady-state convection, and their surface topographies can be compared. Visual inspection of the results at the final time step confirms that low tracer densities (best seen in the 10 or 20 tracer per cell models in Figure **??**) result in grainy, unrefined topography, while increasing tracer density results in much smoother topography, which would be expected in a constant viscosity model.

The quality of surface topography using the marker-in-cell method is strongly dependent on number of tracers per cell (TPC). Low tracer densities result in grainy, unrefined topography, with the quality of the topography increasing with tracer density. The magnitude of topography is a dimensionless fraction of the total mantle thickness (normalised to 1).

While visually apparent, it is also possible to quantify the noise present at different tracer densities by computing the distribution of surface topography. Figure **??** shows this distribution for a selection of tracer densities as computed by sampling the surface topography of each model at all time steps, excluding the first 200 in order to avoid including the initial warm-up period before steady-state convection is reached. The results show a distribution of topography slightly skewed above the initial level (0.0), which is consistent with visual inspection of Figure **??** that shows the majority of topography is above the initial level with relatively small cold plumes forming deeper topographic lows. The key result is that the distribution is much wider at lower tracer densities, indicating the presence of noise in the topography data. The amount of noise appears to become smaller with increasing tracer density, until the point where it is reasonable to assume the amount of noise is negligible at 500 tracers per cell. Further increases beyond this tracer density differ minimally.

Surface topography probability density function averaged over all timesteps for the five models as shown in Figure **??**. At low tracer densities, the distribution is relatively wide indicating that the noise that is more apparent with low marker densities is affecting the quality of the topography generated.

~~This result demonstrates that a trivial solution to achieve greater topographic resolution is to increase the tracer density. However, this is not always possible in large scale 3D models due to computational limitations. For the same models as above, we compare the computational effort (measured in total computational time), as a function of tracers per cell (Figure ??). Tracers are advected using a 4th-order Runge-Kutta scheme with velocities interpolated to tracer locations using a divergence-free quadratic spline method, while the Stokes and continuity equations are solved using a geometric multigrid solver (Tackley, 2008). These results show a linear dependence of computational effort involved in advecting tracers with tracer density. Memory usage also scales linearly. While this computational trade-off is reasonable for relatively fast and low resolution models such as this one, when scaling to much larger models the computational effort involved in advecting tracers can quickly dominate, which presents a major limitation when attempting to model topography accurately on the global scale. In the models run for Figure ??, tracer computation accounted for 9% of total runtime at 10 tracers per cell, and 77% at 500 tracers per cell, with the 50% crossover point occurring between 100 and 150 tracers per cell.~~

~~Tracer density (measured in tracers per cell) is linearly correlated with the total runtime of tracer calculations in the model (total CPU time in seconds, 8 CPU cores, AMD Ryzen 9 3900XT). At higher tracer densities, tracer computation time exceeds the computation time of the Stokes solver, becoming the largest component of total runtime. In this example, tracer computation accounts for between 9% of total runtime at 10 tracers per cell, and 77% at 500 tracers per cell.~~

~~These findings highlight the limitations of the marker-in-cell method for tracking surface locations. Developing a tracer density independent method is critical for improving topographic accuracy while reducing computational cost in global-scale geodynamic models.~~

2 Surface tracking

2.1 Marker chain/mesh

In 2D models, the surface can be tracked by a marker chain which is initialised as an ordered array of Lagrangian markers, each of which stores its position $\mathbf{x}_i$ and a type variable to facilitate manipulation of the chain. The position vector for each marker $\mathbf{x}_i$ may be represented in either Cartesian coordinates $\mathbf{x}_i = (x_i, z_i)$, or polar coordinates ~~$\mathbf{x}_i = (r_i, \theta_i)$~~ $\mathbf{x}_i = (r_i, \phi_i)$, and may be dimensional or dimensionless. The height of each marker (z_i or r_i) is set by an initial surface height function $z_{\text{init}}(x)$ or ~~$r_{\text{init}}(\theta)$~~ $r_{\text{init}}(\phi)$.

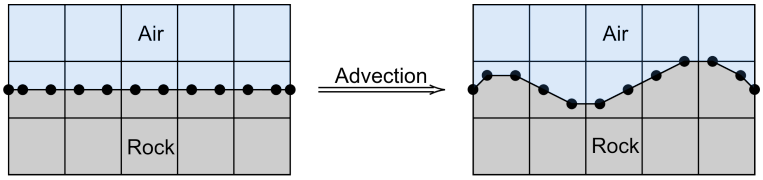

Figure 1. The marker chain divides the domain into regions ~~or~~ of rock and air. Lagrangian markers are advected with the velocity field at each timestep to model the evolution of the surface over time.

In 3D models the surface representation extends to a mesh. The initial surface consists of markers arranged in a grid with coordinates $\mathbf{x}_i = (x_i, y_i, z_i)$ in Cartesian geometry, or $\mathbf{x}_i = (r_i, \theta_i, \phi_i)$ in spherical geometry. As with the 2D case, the initial height of the markers z_i or r_i is given by an initial surface height function $z_{\text{init}}(x, y)$ or $r_{\text{init}}(\theta, \phi)$.

Surface markers are advected with the velocity field, determined from the Stokes solver, using a spatially fourth-order Runge-Kutta scheme, similar to the treatment of the ~~tracers~~ markers used in StagYY. Velocities, which are face-centred in the staggered-grid finite-volume discretisation used by StagYY, are interpolated to surface markers using a second-order quadratic spline interpolation method (Gerya et al., 2021).

2.2 Piecewise linear ~~/bilinear~~ surface reconstruction method (bilinear method)

It is necessary to be able to determine the location of the surface as a function of position through interpolation, i.e. finding $z(x)$ or ~~$r(\theta)$~~ $r(\phi)$ in 2D, or $z(x, y)$ or $r(\theta, \phi)$ in 3D as a function of the position of the Lagrangian surface markers. A straightforward approach is to construct a piecewise continuous linear or bilinear representation of the surface using a first-order accurate distance-weighted linear interpolation (Gerya, 2019)(Chapter 18). This method was employed with a 2D marker chain in the context of modelling free surfaces in numerical geodynamic models by Duretz et al. (2016), and a similar method is used in 3D models using the regional scale geodynamic code LaMEM (Kaus et al., 2016). The method requires two steps: the interpolation of surface height data from Lagrangian surface markers to nodal points using distance-weighted linear interpolation, and the linear or bilinear interpolation of nodal values to arbitrary locations within the domain. Once surface heights are interpolated to nodes, determining the surface height at any point can be accomplished in constant $O(1)$ time, independently of the number of surface markers.

For consistency, this approach is referred to throughout ~~this chapter~~ as the *bilinear method*, reflecting the bilinear interpolation used in 3D models. In 2D, the process is technically linear, but the term *bilinear method* is retained for uniformity.

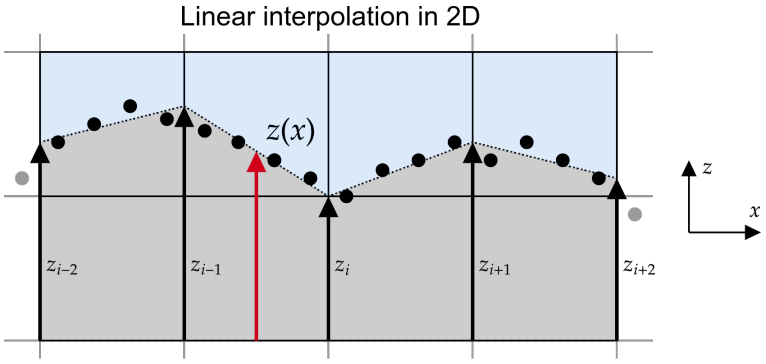

Figure 2. When using the ~~linear/~~bilinear representation of the surface, the surface markers are interpolated to the nodes of the Eulerian grid through distance-weighted linear interpolation. The surface height at a given point e.g. $z(x)$ (red arrow) may then be computed using linear interpolation.

2.2.1 ~~Interpolating surface markers to nodes~~

~~Interpolation of surface heights from markers to the nodes of the Eulerian grid (denoted by z_i) in 2D models is carried out using a 1D distance-weighted linear interpolation (Gerya, 2019):~~

$$z_i = \frac{\sum_m z_m w_{m(i)}}{\sum_m w_{m(i)}},$$

$$w_{m(i)} = 1 - \frac{\Delta x_m}{\Delta x}.$$

~~Where z_m is the height of the m'th surface marker, $w_{m(i)}$ refers to the weight of the m'th surface marker for the i'th node, Δx_m denotes the distance from the m'th surface marker to the i'th node, and Δx denotes the grid spacing. Each node is interpolated using only surface markers found within one grid spacing Δx of the node. In 3D, the method can be extended to determine surface heights at nodes denoted by $z_{i,j}$:~~

$$z_{i,j} = \frac{\sum_m z_m w_{m(i,j)}}{\sum_m w_{m(i,j)}},$$

$$w_{m(i,j)} = \left(1 - \frac{\Delta x_m}{\Delta x}\right) \times \left(1 - \frac{\Delta y_m}{\Delta y}\right)$$

~~Where z_m is the height of the m'th surface marker, $w_{m(i,j)}$ refers to the weight of the m'th surface marker for the i,j'th node, Δx_m and Δy_m denote the x and y distances from the m'th marker to the i,j'th node, and Δx and Δy denote the grid spacing.~~

~~When using spherical coordinates, r,θ, and ϕ may be directly substituted for z,x, and y in the above to obtain the surface height at nodal points r_i or $r_{i,j}$.~~

~~In both 2D and 3D, the performance of this operation scales linearly $O(n)$ with respect to the number of surface markers n.~~

2.2.1 ~~Linear/bilinear interpolation~~

2.3 Direct interpolation (integral method)

~~In the second step of surface reconstruction, the location of the surface~~ Another method of determining the surface location at arbitrary points ~~in the domain can be determined by interpolating between nodal values. This is achieved by using linear interpolation in 2D, or bilinear interpolation in 3D (Equations **??**, **??**).~~ is through direct interpolation from the marker chain or mesh, without first mapping to the Eulerian grid. In 2D~~, to interpolate the surface height at a point $z(x)$, the surface heights at the neighbouring nodes to the left and right are used:~~

$$z(x) = \frac{1}{\Delta x}\left(z_i(x_{i+1} - x) + z_{i+1}(x - x_i)\right),$$

Where x_i and x_{i+1} represent the x coordinate of the nodes immediately to the left and right of the point x, z_i and z_{i+1} are the surface heights at those nodes, and Δx is the gridspacing.

In 3D models, four nodes which form a quadilateral surrounding the point of interest must be used to construct a bilinear interpolation of the surface location $z(x,y)$, with their locations denoted by (x_i,y_j), (x_{i+1},y_j), (x_i,y_{j+1}), and (x_{i+1},y_{j+1}). The bilinear interpolation of the surface is then given by:

$$z(x,y) = \frac{1}{\Delta x \Delta y}(z_{i,j}(x_{i+1}-x)(y_{j+1}-y) + z_{i+1,j}(x-x_i)(y_{j+1}-y) + z_{i,j+1}(x_{i+1}-x)(y-y_j) + z_{i+1,j+1}(x-x_i)(y-y_i)).$$

Again, when using spherical coordinates, r,θ, and ϕ may be substituted directly for z,x, and y in the above to obtain the surface height at nodal points $r(\theta)$ or $r(\theta,\phi)$.

For both 2D and 3D cases, this operation is independent of the number of surface markers, and can be accomplished in constant $O(1)$ time.

2.4 Direct interpolation in 2D (integral method)

Another method of determining the location of the surface $z(x)$ or $r(\theta)$ in 2D at arbitrary points within the domain is through directly interpolating the surface location from the marker chain. This can be this is achieved by locating the markers on the chain that are immediately to the left and right of the interpolation point , and then linearly interpolating the surface height between these two points.

In Cartesian coordinates, linear interpolation of $z(x)$ at the point x located between the surface marker lying immediately to the left $\mathbf{x}_i = (x_i, z_i)$ and right $\mathbf{x}_{i+1} = (x_{i+1}, z_{i+1})$ of x is accomplished using:

$$z(x) = \frac{z_i(x_{i+1}-x) + z_{i+1}(x-x_i)}{x_{i+1}-x_i}.$$

It is possible for higher order interpolation methods to be used to interpolate the marker chain such as a piecewise quadratic interpolation, and linearly interpolating between them. Higher order methods such as piecewise quadratic or cubic spline interpolation . In practice however, adequate results can be achieved with a are possible, but in practice simple linear interpolation without recourse to higher order methodsproduces adequate results.

2.3.1 Sorting the marker chain in 2D

In order to directly interpolate on the chain, it is necessary to locate the markers on the chain immediately to the left and right of a given point. In order to efficiently do this, a $O(\log n)$ binary search can be used which requires the chain to be sorted by the horizontal coordinate. As advection of the surface markers allows them As advection allows markers to move laterally, it is possible for the chain to become disordered over time, necessitating a sorting step after every timestep. As the chain must be

re-sorted by horizontal coordinate after each timestep. Since the chain is ~~often fully or nearly fully~~ typically nearly sorted after advection, adaptive ~~sorting~~ algorithms such as insertion sort are ~~well-suited for maintaining the order of the chain~~efficient for this purpose, and an $O(\log n)$ binary search can then be used to locate neighbouring markers for interpolation.

2.4 ~~Direct interpolation in 3D (integral method)~~

~~Direct interpolation of the marker mesh in~~ In 3D~~is more difficult, as~~, direct interpolation is more involved since the surface is ~~no longer represented with lines, but with planes defined by the points of the marker mesh~~represented by planes rather than line segments. As the surface markers are generally unstructured, ~~this necessitates the use of a meshing algorithm such as Delaunay triangulation.~~

~~In 3D, Lagrangian markers are advected with the velocity field, and the Delaunay triangulation recomputed at each timestep in order to create a mesh which continuously tracks the surface.~~

~~The Delaunay triangulation is computed in 2D using the horizontal (x_i, y_i) coordinates of each marker , not including the height coordinates z. In spherical geometry it~~ a Delaunay triangulation of the horizontal marker coordinates is used (Figure 3). The triangulation is computed using ~~(θ_i, ϕ_i) coordinates for simplicity. This leads to minor errors in the Delaunay triangulation from projecting the spherical patch into a Cartesian plane, but these errors are negligible due to the limited range of θ used by the yin-yang grid. Additionally, the triangulation itself does not have to satisfy the Delaunay criteria, as any triangulation of the surface marker mesh is sufficient for the purposes of this study~~GEOMPACK2 (Joe, 1991) in $O(n \log n)$ time and must be recomputed at each timestep; adaptive methods exist to reduce this cost (Phongthanapanich and Dechaumphai, 2004). Methods for performing Delaunay triangulations directly on spheres also exist ~~, for example Renka (1997).~~

~~Computing the Delaunay triangulation of n surface markers can be performed in $O(n \log n)$ time using an efficient divide and conquer method as employed by GEOMPACK2, while the naive incremental method takes $O(n^2)$ (Joe, 1991).~~

~~The Delaunay triangulation must be computed at each time step to preserve the properties of the triangulation as markers may move relative to one another due to advection. Algorithms for adaptive Delaunay triangulation exist which are able to exploit the fact that typically after an advection step, the existing triangulation will be close to the Delaunay triangulation (Phongthanapanich and Dechaumphai, 2004).~~

2.3.1 ~~Interpolation of the mesh~~

~~An efficient~~ (Renka, 1997), though for the yin-yang grid (Tackley, 2008) the errors introduced by projecting the spherical patch into a Cartesian plane are negligible. Each Delaunay triangle defines a plane through three markers $\mathbf{a}, \mathbf{b}, \mathbf{c}$, with normal vector $\mathbf{n} = (\mathbf{b} - \mathbf{a}) \times (\mathbf{c} - \mathbf{a})$, from which the surface height at any point within the triangle can be recovered. An efficient $O(\log n)$ ~~method exists in~~ triangle location method is available in GEOMPACK2~~for looping through a Delaunay triangulation to locate the (2D) triangle that encloses a given point (x, y) if such a point exists (Joe, 1991). This Delaunay triangle corresponds to three markers in 3D, $\mathbf{a}$, $\mathbf{b}$, and $\mathbf{c}$, which together define a plane .~~

~~This plane can be defined through the equation $\mathbf{n} \cdot \mathbf{x} = \alpha$, where $\mathbf{n}$ is a normal vector and α is a scalar value. The normal vector $\mathbf{n}$ can be derived from the three points as:~~

$$\mathbf{n} = (\mathbf{b} - \mathbf{a}) \times (\mathbf{c} - \mathbf{a}).$$

With some rearrangement, the equation of this plane allows for determination of surface height $z(x, y)$ as a function the three points in the triangulation (as shown in Figure **??**):

$$z(x, y) = \frac{n_x(a_x - x) + n_y(a_y - y)}{n_y} + n_y a_y.$$

Similarly, in spherical geometry $r(\theta, \phi)$ can be given by:

$$z(\theta, \phi) = \frac{n_\theta(a_\theta - \theta) + n_\phi(a_\phi - \phi)}{n_\phi} + n_\phi a_\phi.$$

Interpolation of the marker mesh within one triangular surface mesh element in 3D Cartesian geometry.

If the point of interest (x, y) ; if the point lies outside the Delaunay triangulation, extrapolation of the nearest Delaunay triangulation, the nearest triangle is used using the same method with the nearest triangle to the pointfor extrapolation.

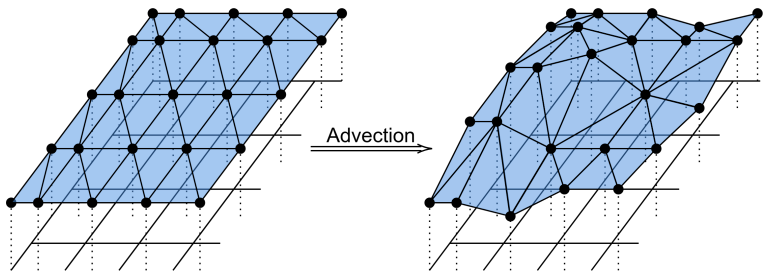

Figure 3. In 3D, Lagrangian markers are advected with the velocity field, and the Delaunay triangulation recomputed at each timestep in order to create a mesh that continuously tracks the surface.

2.4 Interpolating to the Eulerian grid

In order to couple the surface tracking method to the Stokes solver and to output the results, it is necessary to interpolate results, the surface heights of the marker chain /mesh or mesh must be interpolated to the Eulerian grid. When using the bilinear method, this step is handled automatically by interpolating surface heights to the nodes of the Eulerian grid. When using For the integral method, there are several possible methods for interpolating to the grid. In this study, a cellwise integration approach was is used in both 2D and 3D.

2.4.1 ~~Cellwise integration~~

The cellwise integration method ~~is to compute~~ computes the area (in 2D) or volume (in 3D) enclosed by the surface within ~~the~~ each computational cell, and ~~to then compute~~ derives the equivalent topographic height ~~in that cell~~ that preserves this area or volume. This is physically motivated by the need to maintain conservation of mass of both rock and air within the model.

In 2D ~~, the surface height z_i is a given cell is given as a function of surface location $z(x)$ by:~~

$$z_i = \frac{1}{\Delta x} \int_{x_{i,l}}^{x_{i,r}} z(x)\, dx,$$

~~Where $x_{i,l}$ and $x_{i,r}$ are the left and right horizontal boundaries of the i'th cell, and $\Delta x = x_{i,r} - x_{i,l}$ is the grid spacing. The numerical integration of $z(x)$ is performed~~ the integral is evaluated using the trapezium rule by looping over ~~all the intervals of points in the marker chain , computing the area under each interval, and adding that area to the correct cells before dividing by grid spacing to obtain the surface height. As the marker chain is already sorted by horizontal coordinate, the integration can be~~ marker chain intervals, which is accomplished in linear time ~~($O(n)$) and with no additional array allocations, and also works where~~ as the chain is ~~sparse.~~

~~A similar concept can be applied for 3D models by evaluating the volume underneath the surface~~already sorted. In 3D~~Cartesian coordinates, the surface height in the i, j'th cell $z_{i,j}$ is given by:~~

$$z_{i,j} = \frac{1}{\Delta x \Delta y} \iint_{C_{i,j}} z(x,y)\, dA,$$

~~Where $C_{i,j}$ denotes the domain of the i, j'th cell.~~

~~Numerically computing the integral can be accomplished by looping through the list of Delaunay triangles , and then applying a polygon intersection algorithm to compute the intersection between the current triangle and~~ , Delaunay triangles are intersected with the footprint of each ~~column of cells (Figure 4). Polygon intersections can be computed efficiently in linear time using an algorithm such as the Sutherland-Hodgman algorithm or O'Rourke et al. (1982). Once the intersection polygon has been determined, it can be split up into triangles with vertices a, b, and c, the heights recomputed from the equation of the plane through the original three points, and the volume of each triangular prism can be computed . Finally, the sum of all triangular prisms in each column of cells can be summed up and divided by the basal area of the column of cells~~ cell column using a polygon intersection algorithm (O'Rourke et al., 1982); the volume beneath each intersection polygon is then computed and summed to obtain the surface height ~~in each column .~~

~~Piecewise integration under the Delaunay mesh using a polygon clipping algorithm is used to compute the volume enclosed by the surface within a given computational cell.~~

~~This operation can be accomplished in linear time~~ per column (Figure 4). Both 2D and 3D operations scale as $O(n)$ with respect to the number of surface markers~~by simply looping through all Delaunay triangles, albeit with some overhead associated with the need to use polygon intersection~~.

2.5 ~~Parallelisation~~

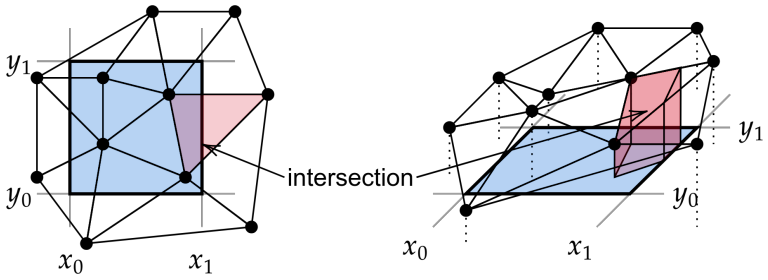

Figure 4. Piecewise integration under the Delaunay mesh using a polygon clipping algorithm is used to compute the volume enclosed by the surface within a given computational cell.

When solving on multiple CPU cores, the ~~model~~ domain is split ~~up into a number of~~ into parallel subdomains. ~~These subdomains are not independent of one another, and certain operations such as passing tracers or fields from one subdomain to the other require the use of Message Passing Interface (MPI).~~

~~For the purposes of interpolation of surface markers, it is not sufficient to use the existing treatment used for tracers in the model, as this could potentially leave a region within the domain where the surface is not defined. It is therefore necessary to exchange more tracers in order to create an overlap region for the purposes of this interpolation. By adapting existing methods for passing regular tracers to exchange this~~ Surface markers near subdomain boundaries are exchanged via MPI to form a one-cell-wide overlap region, ~~it is possible to form this overlap region such that~~ ensuring the surface is defined at all locations ~~within the domain~~ for all subdomains (Figure 5).

3 Stabilisation

When implemented naively, the surface marker chain/mesh does not satisfy the criterion of being stable over multiple timesteps. There are three main reasons for this. Firstly, while the solution to the Stokes equations ~~ensure~~ ensures conservation of mass, the surface marker chain/mesh itself ~~is not~~does not, and may shift up and down over time~~, causing errors in mass conservation~~. Secondly, regions of divergence can cause the surface markers to become widely spaced, compromising ~~the accuracyof the method~~accuracy. Thirdly, regions of convergence can cause entrainment of markers into the mantle, a feature which is unphysical and must be corrected (Figure 6). There are several ways that these stability issues can be addressed.

3.1 ~~Surface height adjustment~~

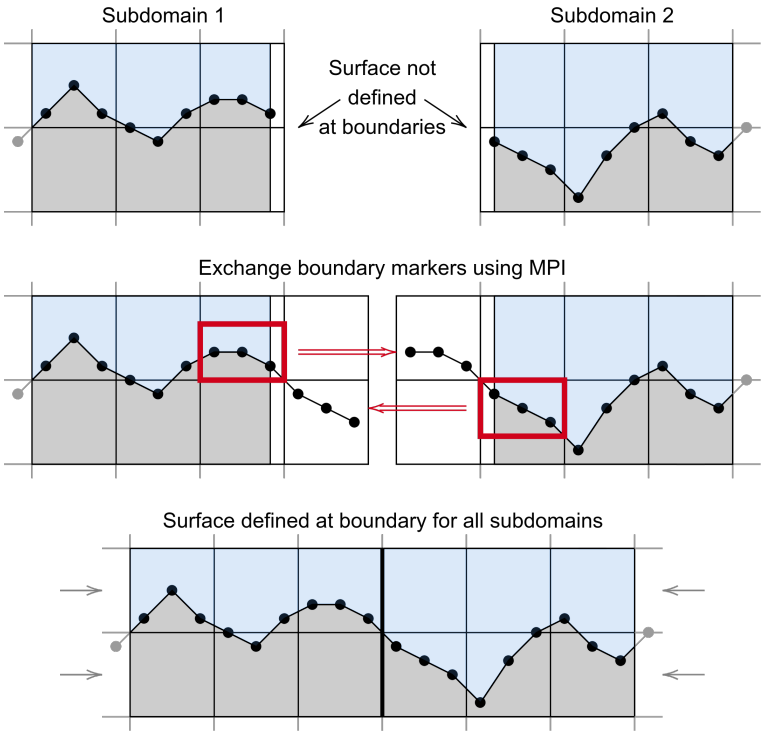

Figure 5. Parallelisation of the marker chain/mesh involves the use of an overlap region ~~which is~~ communicated between subdomains ~~. As the surface itself is not necessarily defined at subdomain boundaries when using markers within the same subdomain, a one cell wide overlap region is taken from the adjacent subdomain. Communication of surface markers between subdomains is achieved using~~ via MPI. This approach is also applicable to 3D cases.

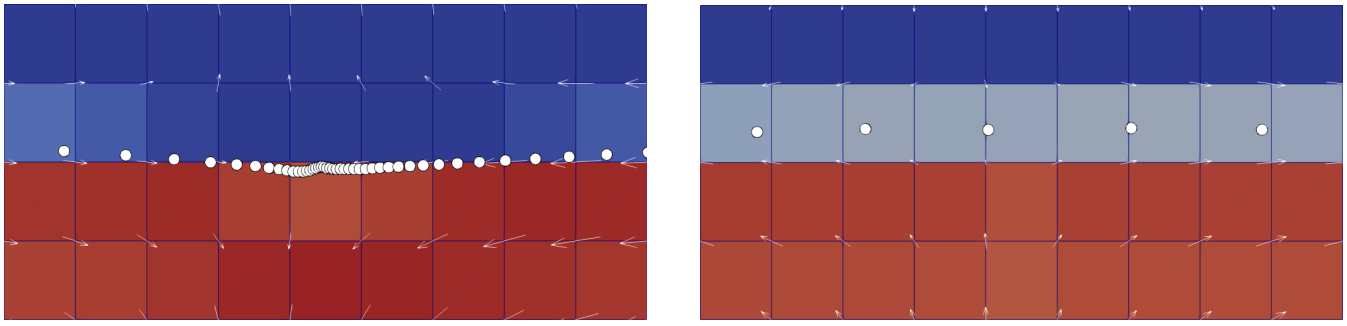

(a) Convergence (b) Divergence

Figure 6. Without reinitialisation, regions of convergence experience bunching of the surface markers, while in regions of divergence the marker density becomes low. These effects must be corrected using reinitialisation to maintain surface marker density.

~~While total mass of rock and air is supposed to be conserved in the numerical model, a fact that should be reflected in the solution to the Stokes equations, it is possible for minor errors to accumulate, which may shift the surface up or down~~

3.1 Surface height adjustment and reinitialisation

Minor numerical errors in the Stokes solution and/or marker advection can cause the surface to drift upward or downward over time. ~~The first stabilisation method adjusts~~ To correct this, the height of ~~the surface markers~~ all surface markers is adjusted at each timestep to preserve the total area or volume of rock and air in the model, and therefore mass ~~assuming near incompressibility of the rock. This can be achieved by integration under the marker chain/mesh.~~

3.1.1 ~~Integral correction~~

~~As the distribution of surface markers is not necessarily even, a more accurate method of ensuring that the volume of rock and air in the model remains the same is by computing the total area/volume under the surface through integration.~~

~~In 2D, the integral correction takes a similar form to that presented for cellwise integration of volume fractions in Section ??.~~

$$z_{i,\text{new}} = z_i - \frac{1}{L_x}\int_{x_L}^{x_R} z(x)\,dx - z_{\text{init}},$$

~~where x_L and x_R denote left and right boundaries of the domain, respectively, and L_x is the total domain width. Similarly to the situation for cellwise integration,~~ under the assumption of ~~surface displacements being small a simplified approximate form of the integral term can be derived, resulting in an expression for the integral surface correction in spherical geometries:~~

$$r_{i,\text{new}} = r_i - \frac{1}{L_\theta}\int_{\theta_L}^{\theta_R} r(\theta)\,d\theta - r_{\text{init}}.$$

~~With left and right domain boundaries θ_L and θ_R, and domain width (in terms of θ) L_θ. In both Cartesian and spherical geometries this integral can be evaluated analytically in linear time when using a sorted marker chain.~~

~~These integrals can easily be obtained in linear time by looping through each interval on~~ near-incompressibility. This is achieved by integrating under the marker chain or ~~nodes and adding up the total area underneath the surface using the trapezium rule.~~

~~When extending the method to 3D, a similar method can be used to the above, however the required integral becomes a volume integral over the entire domain, which is then divided by the total area of the domain. These volume integrals in Cartesian and spherical coordinates are given by:~~

$$V = \iint_D z(x,y)\,dA \quad \text{in Cartesian coordinates,}$$

$$V = \iint_D r(\theta,\phi)\,dA \quad \text{in spherical coordinates}$$

~~Which should remain constant for all timesteps to ensure that volume conservation is achieved.~~

~~While in Cartesian coordinates the infinitesimal area dA is simply given by $dA = dy\,dx$, in spherical coordinates the area correction must be derived from the definition of an infinitesimal surface element (Kreyszig, 2010):~~

$$dA = \left\| \frac{\partial \mathbf{r}}{\partial \theta} \times \frac{\partial \mathbf{r}}{\partial \psi} \right\| d\theta\, d\phi = \left| r\hat{\boldsymbol{\theta}} \times r\sin\theta\hat{\boldsymbol{\phi}} \right| = r^2 \sin\theta\, d\theta\, d\phi,$$

$$\text{where } \mathbf{r} = \begin{bmatrix} r\sin\theta\cos\phi \\ r\sin\theta\sin\phi \\ r\cos\theta \end{bmatrix},$$

~~Where setting $r = R$, the radius of the planet, obtains the infinitesimal area near the surface.~~

~~These integrals are evaluated similarly to the cell integration method presented~~ mesh using the same trapezium rule or Delaunay-based approach described in Section 2.4. ~~When using a Delaunay triangulation, it is possible to loop over all Delaunay triangles using a polygon intersection algorithm to isolate the parts of triangles which are within the modelling domain, and then to compute the volume of each triangular prism underneath. A correction for variable dA can then be applied for the case of spherical geometry. This is relatively efficient, and can be evaluated in linear time with respect to the number of Delaunay triangles.~~

~~When using the bilinear method, the integral can be easily evaluated using a weighted sum of the nodal surface heights~~, with corrections for ~~varying dA as needed.~~

~~This method runs in linear time ($O(n)$) with respect to the number of surface markers~~the spherical area element $dA = r^2 \sin\theta\, d\theta\, d\phi$ (Kreyszig, 2010) applied where necessary.

~~(a) Convergence (b) Divergence Without reinitialisation, regions of convergence experience bunching of the surface markers, while in regions of divergence the marker density becomes low. These effects must be corrected using reinitialisation to maintain surface marker density.~~

Although reinitialisation is essential for preserving the integrity of the marker chain over multiple ~~time steps~~timesteps, it does come with trade-offs~~. Specifically,~~ : the process may degrade information about the surface geometry and introduce artificial numerical diffusion. Therefore, reinitialisation should only be applied when needed~~to avoid excessive smoothing~~.

3.1.1 ~~Periodic global reinitialisation~~

~~One of the simplest reinitialisation strategies is periodic global reinitialisation. In this approach,~~ Two reinitialisation strategies are implemented. The first is *periodic global reinitialisation*, in which the entire surface marker chain/mesh is reinitialised to align with the current surface level ~~using one of the interpolation methods described earlier or based on the Eulerian representation of the surface.~~

~~Periodic global reinitialisation~~ at every timestep. This is computationally efficient ~~, as it~~ and maintains a consistent number of surface markers~~. However, a significant drawback is the loss of surface information and the introduction of numerical diffusion into the model. For instance, global reinitialisation can overly~~ , but introduces numerical diffusion that can smooth surface features ~~, as can be demonstrated when using a test case with an initially sinusoidal surface~~ over time (Figure 7). ~~In this test, the markers are not advected with the velocity field, but are smoothed at each timestep due to the use of periodic global reinitialisation at each timestep~~It does not require the chain to be sorted or the Delaunay triangulation to be computed, making it compatible with the bilinear method. Despite the diffusion it introduces, some smoothing is beneficial for stability, and the effect is relatively mild in practice.

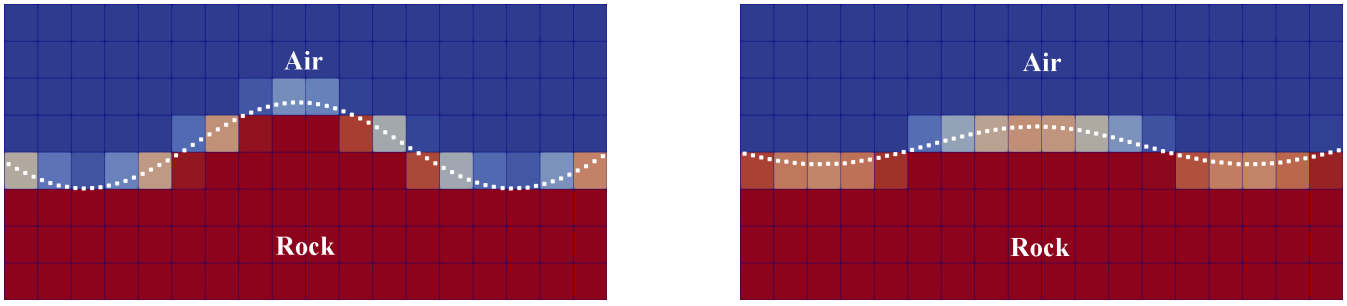

(a) Timestep 1 (b) Timestep 20

Figure 7. Illustration of the smoothing effect caused by global periodic reinitialisation over 20 timesteps using bilinear interpolation. There is no coupling between the surface marker chain and the underlying model; all deformation of the surface is caused by numerical diffusion resulting from global reinitialisation.

~~Despite these limitations, periodic global reinitialisation of surface markers does not require the marker chain/mesh to be previously sorted (or the Delaunay triangulation to be computed), making it suitable for use in conjunction with the bilinear interpolation method. Additionally, while it can reduce the fidelity of some small scale topographic variations, some level of smoothing may be beneficial, as it would otherwise have to be introduced deliberately to maintain surface stability. However, balancing this smoothing effect with the need to preserve surface details remains a challenge.~~

~~Global reinitialisation can be accomplished in linear time $O(n)$ when used in conjunction with the bilinear method, and $O(n \log n)$ when used in conjunction with direct interpolation methods due to the $O(\log n)$ time required to sample the surface height at a given location with those methods.~~

3.1.1 ~~Interval reinitialisation~~

Interval based reinitialisation in 2D is The second strategy is *interval reinitialisation*, in which markers are added or removed locally based on the interval spacing between adjacent markers . If the interval exceeds the maximum interval size, which is a user-defined limit proportional to the original marker spacing Δx_{init}(in 2D) or the area of Delaunay triangles (in 3D). In 2D, a marker is added to the chain at the midpoint of the interval. If the interval is too small, the two markers that make up the interval are merged into one at the midpoint of the interval. It is desirable to have an upper threshold no greater than 2 to ensure that markers are added at the same or greater density as the initial starting density, and a lower threshold sufficiently small to allow markers to bunch up in regions where it is needed subduction zones, but not so large as to introduce large numbers of new markers into the model. Empirical testing found that the thresholds $0.2 \leq \Delta x / \Delta x_{\text{init}} \leq 2$ provides any interval exceeding $2\Delta x_{\text{init}}$, and two markers are merged if their spacing falls below $0.2\Delta x_{\text{init}}$; empirical testing confirmed these thresholds give good results.

In The 3D , a similar concept is applied to the areas of the Delaunay triangles. In cases where the ratio of triangle area to initial analogue uses triangle area ratios A/A_{init} exceeds a certain amount, a new marker is introduced at the midpoint in order to subdivide the triangle, while in cases where it is small the three points of the triangle are merged into one at the midpoint. To ensure that markers are added at the same density as the initial density, the upper threshold should be no greater than 3, as with an upper threshold of 3 new triangles are created from each triangle that is subdivided. Likewise the lower threshold should be sufficiently small to enable high resolution but not so small as to introduce large numbers of new markers, affecting performance. Empirical testing found that a range of $0.2 \leq A/A_{\text{init}} \leq 3$ provides good results.

Interval based reinitialisation has the benefit of not modifying the marker chain where it is unnecessary, thus avoiding and a lower threshold of 0.2. This approach avoids the numerical diffusion inherent in global or cellwise reinitialisation schemes. It is relatively efficient; iterating through the markers to check the intervals takes linear time $O(n)$, while inserting a single new marker generally also takes $O(n)$. A downside is that there is an increased upper bound on the number of markers that can be introduced into the model, requiring more memory and computational resources, however, this can be controlled by modifying the lower interval bounds. Additionallyreinitialisation by only modifying the chain where necessary. However, it requires either sorting or Delaunay triangulation of the surface markers, which precludes its use in conjunction with the bilinear method.

3.2 The need for smoothing

A fundamental problem with the Lagrangian surface marker method is the undesirable entrainment of markers into the mantle or air layer instead of remaining at the surface. The effect is most pronounced when using the integral method, and results in the formation of unrealistically deep trenches or high mountains that are not physically reasonable and can result in numerical instabilities in the model can cause numerical instabilities (Figure 8). Solving this problem requires a method of smoothing the Lagrangian markers.

A natural choice for smoothing surfaces is a diffusionprocess. Two key characteristics of diffusion make it a logical choice: it is a conservative process, ensuring that the total amounts of rock and air in the model remain constant, and it is physically motivated, with the material flux being proportional to the slopeis diffusion, which is conservative and physically motivated. However, this approach can add diffusion to the surface unnecessarily, where model features are smoothed out over time as

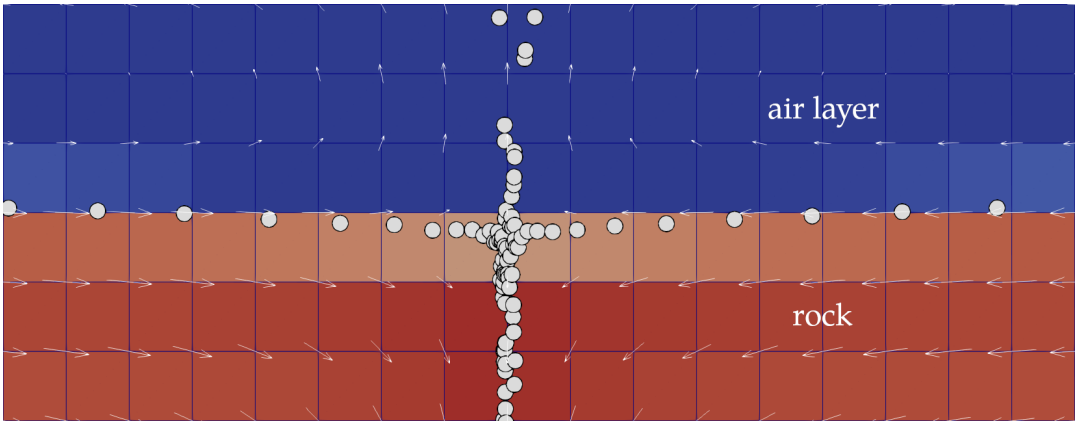

Figure 8. In the absence of an appropriate smoothing algorithm, surface markers can become entrained within rock (red) or the sticky air layer (blue), causing significant numerical instability.

~~a result of diffusion of the marker chain, as opposed to any physical process. As noted above,~~ it can smooth model features unnecessarily, and periodic global reinitialisation, if used, already ~~results in~~ introduces some numerical diffusion.

3.3 ~~Slope limiting~~

~~In an attempt to overcome the limitations of pure diffusion based smoothing, alternative methods of locally smoothing the marker chain/mesh were investigated.~~ The method implemented ~~for smoothing when using~~ here for the integral method is ~~a novel 'slope limiting method'~~ instead a novel slope limiting approach.

~~The physical motivation for the~~

3.3 Slope limiting

The slope limiting method ~~comes from examining the slope of piles~~ is physically motivated by the behaviour of loosely packed ~~materials such as sand. A sand pile under the influence of gravity will naturally form a conical shape with~~ granular materials: a pile of sand under gravity forms a cone with a maximum angle of repose ϕ ~~which is related to its~~ , related to the internal coefficient of static friction ~~μ_s by :~~

$$\tan(\phi) = \mu_s.$$

~~The angle of repose ϕ in typical materials (such as sand) is around 30 - 40°. Materials that are sloped below the angle of repose are stable, while materials which are above are unstable and will~~ by $\tan(\phi) = \mu_s$. Slopes below this angle are stable; those above erode until the angle is reached. ~~Cohesion of the material is not considered in this model.~~

3.3.1 ~~Governing equation~~

~~The behaviour described above can be~~ This behaviour is expressed as a ~~partial differential equation~~ steady-state PDE based on the diffusion equation:

$$\frac{\partial z}{\partial t} = k \frac{\partial^2 z}{\partial x^2} \nabla^2 z \, H \left(\frac{\partial z}{\partial x} ||\nabla z|| - s_{\text{crit}} \right) = 0, \tag{1}$$

where H is the Heaviside step function ~~,~~ and s_{crit} is the critical slope~~, and k is a diffusion coefficient. The effect of the Heaviside function is to ensure that~~ . The Heaviside function ensures that only regions where the slope ~~is below the critical threshold~~ exceeds s_{crit} are ~~not modified. In the implementation, only the steady state form of this equation is considered, which is given by:~~

$$\frac{\partial^2 z}{\partial x^2} H \left(\frac{\partial z}{\partial x} - s_{\text{crit}} \right) = 0.$$

~~This equation extends to 3D by replacing the second derivative of z with $\nabla^2 z = \partial^2 z / \partial x^2 + \partial^2 z / \partial y^2$, and the first derivative with the norm of the gradient. The equation becomes:~~

$$\nabla^2 z \, H \left(||\nabla z|| - s_{\text{crit}} \right) = 0.$$

~~The Heaviside function introduces a nonlinearity to the otherwise linear diffusion equation, which somewhat increases the difficulty of the solution. Iterative methods are able to solve the problem~~ modified, limiting the smoothing effect to regions of high deformation such as subduction or collision zones. The nonlinearity introduced by the Heaviside function is handled using an iterative solver in both 2D and 3D. Applied to sinusoidal test surfaces (Figures 9 and 10), the method flattens steep wave flanks while leaving shallower regions unaffected.

~~The principal effect of slope limiting is to cap gradients at a fixed value. Applied to simple sinusoidal profiles in 2D and 3D (Figures 9 and 10), this flattens the wave sides where gradients peak, mimicking the behaviour of piles of sand.~~ A key advantage ~~is that slope limiting leaves regions unaffected where the gradient does not exceed s_{crit}. This limits the effect to specific regions of high deformation, such as subduction zones or collision zones, where smoothing is necessary to ensure stability. This approach also improves performance when the surface is minimally deformed, as gradient checking can be accomplished in linear time. Additionally, slope limiting~~ of slope limiting over diffusion is that it is timestep independent, ~~unlike diffusion smoothing or bilinear methods, meaning that it will produce the same results over a variety of~~ producing consistent results across different temporal and spatial scales.

3.3.1 ~~Limitations of slope limiting~~

~~A key limitation of the slope limiting algorithm~~ A limitation is its relatively poor ~~performance in both 2D~~ computational performance (see Section 5.6.1), and ~~3D, as can be seen in the performance results presented in Figures 17 and ??.~~

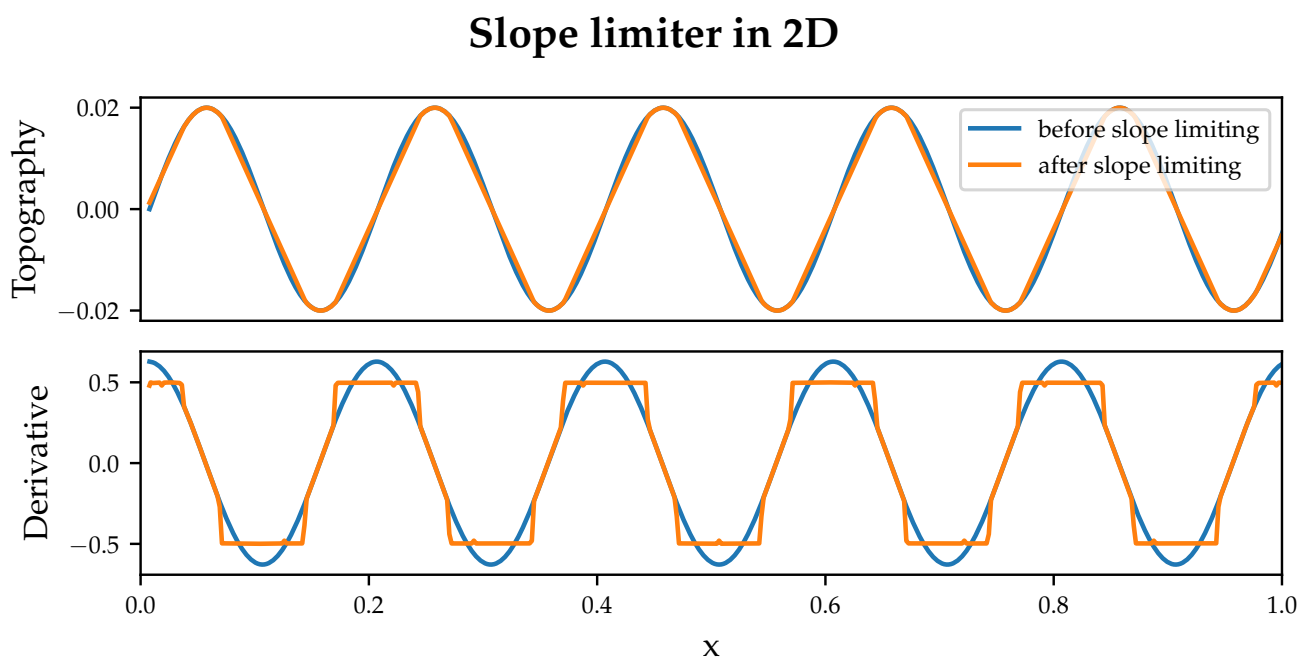

Figure 9. Slope limiter in 2D showing topography (top) before and after the slope limiter has been applied to an initial surface $z = 0.02\sin(5\pi x)$, and its derivative (bottom) showing the limiting of the slope to a maximum of $s_{\text{crit}} = 0.5$.

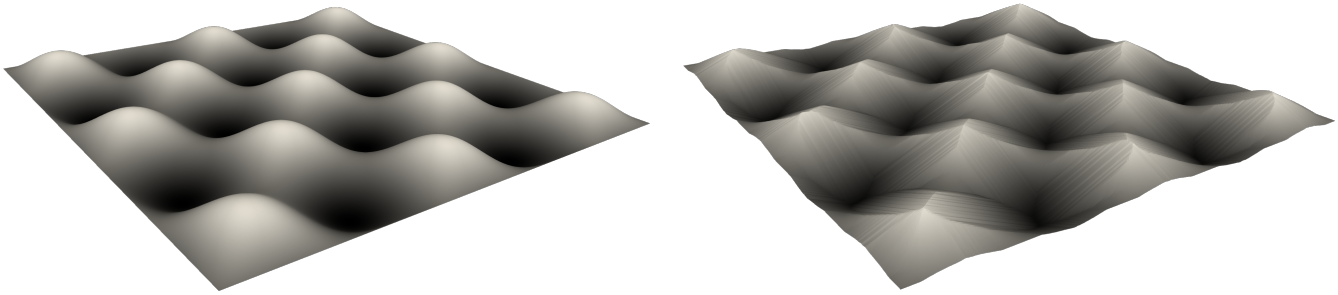

(a) Before slope limiting

(b) After slope limiting

Figure 10. ~~A test on a Cartesian grid showing the effect~~ Effect of the slope limiting algorithm with $s_{\text{crit}} = 0.5$ in 3D on an initial surface $z = 0.05\sin(5\pi x)\sin(5\pi y)$, where $x, y \in [0, 1]$.

~~Another limitation common to all methods of smoothing a surface marker chain/mesh is~~ the fact that it only modifies the ~~location of the surface ,~~ surface location and not the underlying ~~tracers that may exist in the model. A result of modifying the surface location independently of the actions of the velocity field is that tracers~~ markers, which can become unmixed as a result. Solutions to this ~~problem~~ are discussed in Section ~~??~~4.1.

4 Coupling between surface tracking and the Stokes solver

Although it is useful to track the location of the free surface by itself, the utility of the method ~~can be~~ is significantly increased by coupling the ~~representation of the surface~~ surface representation to the mechanical solver such that the height of the surface affects cell-averaged density (hence buoyancy) and viscosity. There are two methods of coupling~~the model to the solver~~: indirectly through manipulation of the existing Lagrangian ~~tracers~~ volumetric markers in the model~~(~~, which then determine the density and viscosity fields~~)~~, and directly through modification of ~~the density and viscosity fields through the use of~~ these fields using volume fraction functions.

4.1 ~~Tracer~~ Marker unmixing

During advection, ~~it is possible for rock tracers to~~ rock markers can end up above the surface ~~, and likewise for air tracers to end up below the surface. This situation~~ and air markers below it. This can also occur ~~if the location of the surface~~ when the surface location is directly manipulated ~~, as it is when applying a smoothing method to the surface. This behaviour is undesirable as it~~ by a smoothing algorithm. The resulting erroneous marker distribution leads to numerical instability ~~,~~ and must be corrected~~by an appropriate method of unmixing erroneous tracers~~. Two methods were implemented ~~to unmix tracers near the surface, tracer bouncing and tracer exchange~~ (Figure 11).

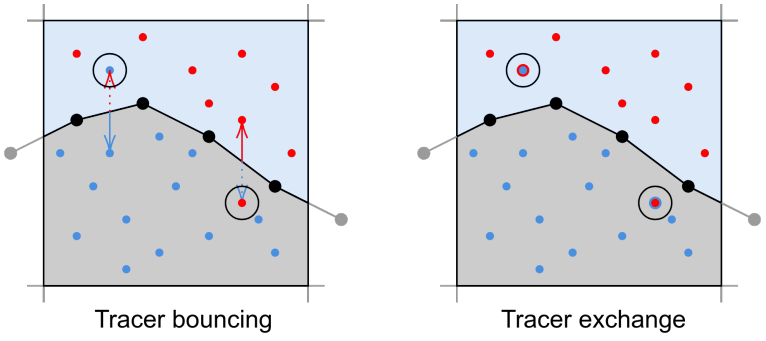

Figure 11. Two methods of dealing with ~~tracers~~ markers which are erroneously on the wrong side of the surface. Air ~~tracers~~ markers (red) should remain above the surface, while rock ~~tracers~~ markers (blue) should remain below. In the bouncing method, erroneous ~~tracers~~ markers (circled) are bounced back to their side, while with the exchange method they are directly converted to the opposite type.

4.1.1 ~~Tracer bouncing~~

~~A simple way of unmixing tracers is to use "bouncing", where erroneous tracers are simply "bounced"~~ In the *bouncing* method, erroneous markers are reflected back to their correct side ~~. In 3D, the bouncing distance is the distance to~~ of the surface, with the displacement equal to their distance from the surface. No markers are created or destroyed, making this method mass-conserving and applicable to models with many marker types. A downside is that bouncing can create gaps in the ~~surface at the x, y position of the tracer:~~

$$z_{\text{new}} = \begin{cases} z(x,y) + |z_{\text{old}} - z(x,y)| & \text{if air tracer below surface} \\ z(x,y) - |z_{\text{old}} - z(x,y)| & \text{if rock tracer above surface} \end{cases}$$

~~A downside of the bouncing method is that it is possible to create gaps where there are no tracers in cases where there is considerable deformation of the surface without motion of the underlying tracers. This problem is particularly apparent~~ marker field in convergent regions ~~,~~ where the surface ~~position is modified through smoothing algorithms~~ is modified by smoothing but the underlying ~~tracers are not. Over time, these gaps can cause severe numerical instabilitydue to the low tracer densities. However, as no tracers are created or destroyed by this method, it conserves total tracer mass and is applicable to cases where many different tracer types are used.~~

4.1.1 ~~Tracer exchange~~

markers are not, which over time can cause numerical instability.

~~Tracer exchange involves exchanging tracers on the opposite side of the surface for~~ In the *exchange* method, erroneous markers are directly converted to the appropriate type~~. Air tracers erroneously~~ : air markers below the surface ~~are directly exchanged for rock tracers, and rock tracers erroneously above the surface are exchanged for air tracers. This method avoids the possibility of large gaps forming near the surface due to tracers being bunched together by~~ become rock markers, and vice versa. This avoids the gap-forming tendency of the bouncing method.

~~While exchanging rock tracers into air tracers is trivial as there is only one type of air tracer, exchanging air tracers to rock tracers require a choice of which type of rock tracer to exchange. The simplest and most efficient choice is to select~~ For the conversion of air markers to rock markers, a random template ~~rock tracer~~ marker is selected from the cell ~~below the free surface. While this method~~ immediately below the surface. This works well for simple ~~model setupswhere the number of unique compositions is small and tracers are not used to advect~~ compositional setups, but becomes unsuitable when markers carry physical properties such as temperature ~~and viscosity, for more complicated setups this method becomes unsuitable due to the potentially large number of potential templates.~~

~~A further caveat to this method is the fact that it is~~ or viscosity, or when many distinct compositions are present. The method is not strictly volume conserving~~due to directly creating and destroying tracer mass through creating and destroying rock and air tracers. On average, however,~~ , though on average the number of ~~rock tracers exchanged for air and air tracers exchanged for rock~~ conversions in each direction remains roughly equal~~, and so total tracer mass is preserved on average, if not on the small scale~~.

4.2 Density and viscosity coupling

StagYY typically ~~uses the marker-in-cell method to calculate~~ determines the density and viscosity fields ~~, which are essential inputs for the Stokes solver. However, with~~ from the marker-in-cell marker distribution. With Lagrangian surface tracking, ~~it is~~

possible to achieve greater accuracy by directly greater accuracy can be achieved by coupling the surface location directly to these fields .

The ability to do so requires the use of volume fractions, denoted by through volume fractions. The volume fraction ϕ . These scalar variables are of a control volume is defined as the fraction of material in a given control volume , with the material for geodynamic applications being rock. The volume fraction function is therefore that volume occupied by rock, ranging from 0 if the control volume is completely empty, and (completely empty) to 1 if it is completely full(Figure 12). In the vicinity of the surface, (completely full), with partially filled cells can be found in which near the surface having $0 < \phi < 1$ (Figure 12).

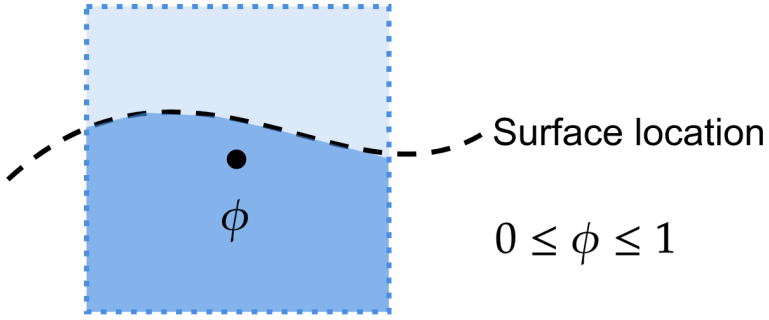

Figure 12. The volume fraction function ϕ for a given control volume is defined as 0 if the control volume is completely empty, and 1 if it is completely full.

StagYY uses a fully staggered grid , where variables are located at different points within the cells (unlike collocated grids). The staggered grid layout in 2D and 3D is illustrated in Figure 13and is (Figure 13), a standard layout in geodynamic modelling (e.g. (Patankar, 1980; Ogawa et al., 1991; Gerya, 2019)). Consequently, volume fractions for specific variables correspond to control volumes offset from the main cells.

The staggered-grid stencil in 2D and 3D used by StagYY. Note that the vertical axis is denoted by z for both 2D and 3D.

In StagYY, (Patankar, 1980; Ogawa et al., 1991; Gerya, 2019), in which the density field is defined for two locations on the staggered grid:

Cell centres (pressure P points) at cell centres and v_z points

Likewise, viscosities are defined , and viscosity at up to four locations on the staggered grid:

(Ppoints , σ_{xz}points σ_{xy} points (, and in 3D only) also σ_{xy} and σ_{yz} points(3D only)). Volume fractions are computed for each of these control volumes offset from the main cells.

As an example, to modify the density field the effective density used in the z-momentum equation to account for the location of the surface, a reference density ρ_{ref} corresponding to the near-surface density of rock, is multiplied by the appropriate volume fraction (ϕ_{v_z}. The resulting effective density z-momentum equation is given by:

$$\rho_{\text{eff}} = \rho_{\text{ref}} \phi_{v_z}, \tag{2}$$

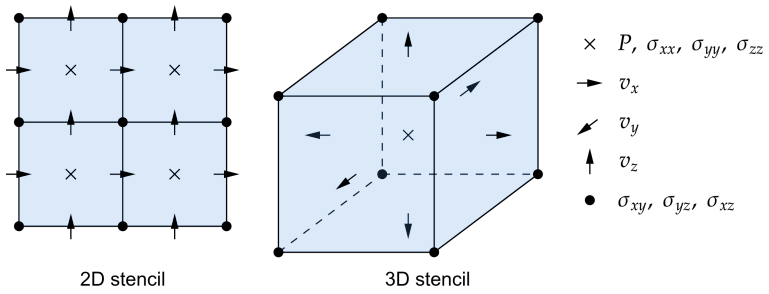

Figure 13. The staggered-grid stencil in 2D and 3D used by StagYY. Note that the vertical axis is denoted by z for both 2D and 3D.

~~Figure 14 illustrates this process for the case of density field modification. Through the use of a volume fraction , this procedure directly incorporates the surface location into the density field~~where ρ_{ref} is a reference near-surface rock density and ϕ_{v_z} is the volume fraction for the v_z control volume (Figure 14). A similar approach ~~can be~~ is applied to the ~~viscosities at the various locationsused in the momentum equations~~viscosity field at each of the relevant staggered grid locations.

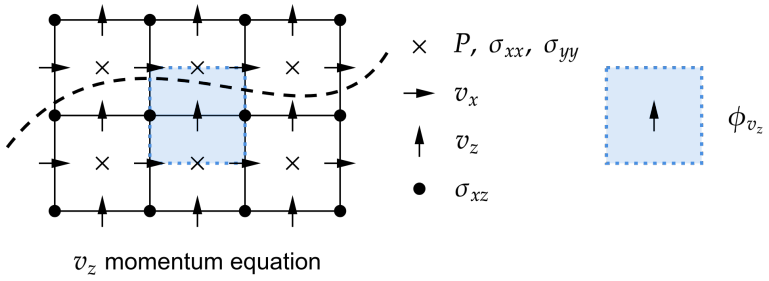

Figure 14. The ϕ_{v_z} volume fraction is used to couple the surface location to the density used in the ~~z-momentum~~ z-momentum equation near the surface.~~A reference density is multiplied by this volume fraction in order to obtain a density that takes into account the location of the surface.~~

~~In order to work properly~~For this to work correctly, the density and viscosity fields must not already include the effect of the sticky air layer, otherwise the ~~effect of an air layer~~ air contribution would be counted twice. ~~It is therefore necessary to set the~~ The air density and viscosity are therefore set to the reference ~~density and viscosity~~values. A caveat ~~of this approach is that it~~ is that this approach does not produce exactly correct results when there are large lateral variations in surface density or viscosity~~, as it is no longer possible to choose a single reference value. A solution to this is to copy reference values~~ ; in such cases, reference values can be copied from the cell immediately below the surface~~; the closest cell that does not contain air~~.

4.2.1 ~~Computing volume fractions~~

~~In 2D, volume~~ Volume fractions are computed geometrically in 2D using the marker chain~~to determine if a cell lies fully below, above, or intersects the surface. This process, conceptually similar to that in Section ??, is efficient with linear time complexity~~

~~$O(n)$. In 3D, the bilinear method allows for exact integration when the surface lies entirely within a single cell, or numerical integration otherwise.~~

~~The integral method in~~ , and in 3D ~~follows a similar approach to that in Section ??, using Delaunay triangles to subdivide the domain into triangular prisms. The volumes of these prisms provide the required volume fractions, also~~ using the same Delaunay-based approach described in Section 2.4, both in linear time $O(n)$.

In all benchmark tests, computing volume fractions incurred negligible cost compared to ~~overall runtime and~~ other surface marker operations.

5 ~~Results~~Tests and results

Three methods ~~, consisting of two Lagrangian surface marker tracking methods and the existing marker-in-cell method,~~ were chosen for testing and benchmarking~~purposes. In order to isolate the effect of surface tracking method, all methods were tested using the sticky air method to approximate the solution of the Stokes equations with a free surface. The methods are:~~

~~The existing method in StagYY, which uses tracers to determine the location of the surface via calculation of a C field using linear shape function averaging. This is the baseline against which potential improvements to surface tracking must be compared. Using~~ : the existing marker-in-cell method (baseline), the *bilinear method* using surface markers with linear~~interpolation of the surface in 2D or~~ /bilinear interpolation in 2D/3D ~~, similar to the method used by Kaus et al. (2016) and Duretz et al. (2016). Using a marker chain or mesh, and evaluating the~~ (Kaus et al., 2016; Duretz et al., 2016), and the *integral method* using cellwise integration to evaluate surface heights on the Eulerian grid~~using~~ . All methods were tested using the sticky air method to isolate the effect of surface tracking. In all benchmarks, 100 volumetric markers per cell are used for the ~~integral method .~~

5.1 ~~2D benchmark summary~~

~~A summary of the default combination of parameters selected for use with each of the five methods in 2D is shown in Table 1. Unless otherwise stated, all~~ marker-in-cell method, a density chosen to represent a reasonable compromise between accuracy and computational cost as demonstrated in the introduction. The same marker population is retained for the Lagrangian methods to ensure a fair comparison by isolating the effect of the surface tracking approach alone. Default parameter combinations for 2D ~~results use these combinations of parameters~~and 3D benchmarks are summarised in Tables 1 and 2.

~~A summary of the 2D benchmarks run can be found in Table ??.~~

5.1 2D relaxation benchmark

The 2D surface relaxation benchmark ~~(Figure ??)~~ is based on Case 1 as presented by Crameri et al. (2012a). It considers the time dependent relaxation of an initially non-flat surface with initial topography $z_{\text{init}}(x)$ given by the function:

Table 1. Summary of Lagrangian surface tracking options used in 2D benchmarks

Method	Surface MPC	Reinitialisation	Smoothing method	Unmixing method
Marker-in-cell	-	-	-	bouncing
Bilinear method	8	global reinitialisation after each timestep	-	bouncing
Integral method	8	interval method $\Delta x/\Delta x_{\text{init}} \in [0.2, 2.0]$	slope limiter $s_{\text{crit}} = 0.5$	exchanging

A summary of the combination of options used for the three methods compared in 2D benchmarks. An initial density of 8 surface markers per cell (MPC) and 100 volumetric markers per cell are used in all 2D models.

Table 2. Summary of Lagrangian surface tracking ~~benchmarks~~ options used in ~~2D~~3D benchmarks

~~Benchmark~~Method	~~Geometry~~Surface MPC	~~Resolution~~Reinitialisation	
~~2D relaxation~~ Marker-in-cell	~~Cartesian~~ -	~~512 × 128~~ -	
~~2D plume~~ Bilinear method	~~Cartesian~~ 16	~~1024 × 256~~ global reinitialisation after each timestep	
~~2D constant viscosity~~ Integral method	~~Spherical annulus~~ 16	~~Various~~ interval method $\Delta x/\Delta x_{\text{init}} \in [0.2, 3.0]$	~~Constant viscosity mod~~

A summary of the combination of options used for the three methods compared in 3D benchmarks. An initial density of $16 = 4 \times 4$ surface markers per cell (MPC) is used in all 3D models.

$$z_{\text{init}}(x) = 7 \cos\left(\frac{2\pi x}{2800\ \text{km}}\right) \text{km}. \tag{3}$$

~~2D surface relaxation benchmark based on Case 1 presented by Crameri et al. (2012a). An initially non-flat surface in a three-layer model relaxes until equilibrium is reached after approximately 100 ky.~~

This problem is simple enough to have an analytical solution for surface position as a function of time as derived using a three-layer model (Ramberg, 1981). Starting from an initial maximum of 7 km, the maximum topography as a function of time $z_{\text{max}}(t)$ is given by:

$$z_{\text{max}}(t) = 7 \exp\left(\frac{t}{14.825\ \text{ky}}\right) \text{km}., \tag{4}$$

where t is time and 14.825 ky is the analytical relaxation timescale derived from the model viscosity structure.

The model domain is a 2800×800 km Cartesian box consisting of three compositional layers: a 600 km thick mantle layer, a more viscous 100 km thick lithosphere, and a 100 km thick air layer. The resolution is 512×128, with 100 ~~tracers~~ markers per cell for advecting material properties and tracking the surface in the case of the marker-in-cell method. The sticky air layer has a viscosity of 10^{18} Pa s. Symmetric boundary conditions are imposed at the horizontal edges of the model, while a no-slip boundary condition is imposed at the bottom boundary, and a free slip condition is imposed at the top. Acceleration due to gravity g is set to 10 m s^{-2}. For consistency with the benchmarks run by Crameri et al. (2012a), models were run until $t = 100$

ky to show the system reaching equilibrium. Timesteps were limited to 500 years in order to give high temporal resolution for plots of model evolution.

The ~~five~~ three surface tracking methods can be compared against the analytical solution when plotting maximum topography with time, as in Figure 15.

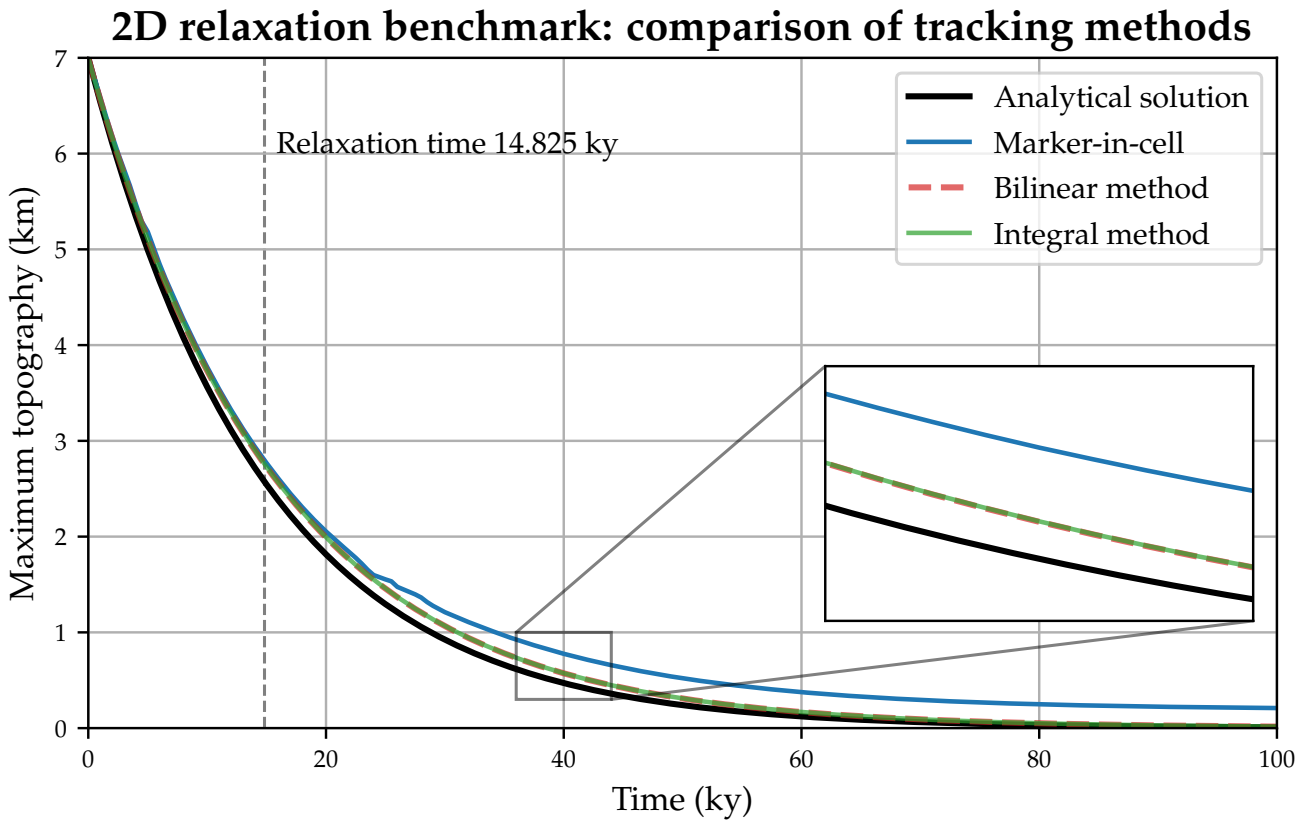

Figure 15. ~~Topography~~ Maximum topography with time for the 2D relaxation benchmark. Both Lagrangian marker based methods closely match the analytical solution. The existing marker-in-cell method, while also tracking the analytical solution closely initially, fails to converge with the analytical solution near the end of the model run.

All methods are qualitatively able to track the analytical solution closely in agreement with the results presented in Crameri et al. (2012a). Minor divergence between the methods becomes more apparent after 30 ky, with the marker-in-cell method failing to match the analytical solution as closely as Lagrangian tracking methods after this point. At 100 ky, while the other methods have converged to a maximum topography near zero, the marker-in-cell method resulted in around 200 m of topography, a result that can also be seen in Figure 2 of Crameri et al. (2012a). This result can be attributed to the maximum topography being affected by the noise inherent in the marker-in-cell method when using a finite number of randomly initialised ~~tracers~~

markers throughout the model. Meanwhile, the Lagrangian surface marker-based tracking methods all converge to near zero at 100 ky, indicating that Lagrangian surface tracking methods are less susceptible to this noise.

It should be noted that part of the remaining discrepancy between the methods presented here and the analytical solution can also be explained by the limitations of the sticky air method (i.e. finite viscosity of air) used to produce the solution to the Stokes equations ~~. Therefore, the remainder of the discrepancy in results may not necessarily be a direct consequence of the surface tracking method~~ rather than the surface tracking method itself. The primary value of this benchmark is therefore in the relative comparison between methods: the Lagrangian tracking methods converge more closely to zero at 100 ky than the marker-in-cell method, demonstrating a clear reduction in marker-density-dependent noise that is independent of the Stokes solver used.

5.2 2D plume benchmark

The 2D plume benchmark ~~(Figure ??)~~ is based on Case 2 presented in Crameri et al. (2012a)~~. It considers a buoyant plume rising through the mantle over a period of 20 My, and the dynamic topography resulting from this plume's impingement on the lithosphere.~~

~~2D plume benchmark based on Case 2 in Crameri et al. (2012a). A buoyant plume rises through the mantle and impinges upon the lithosphere, producing dynamic topography over a time period of 20 My.~~

~~The domain is a 2800 × 850 km Cartesian box domain run at a resolution of 1024 × 256, consisting of three compositional layers: a 600 km thick mantle, a 100 km thick lithosphere, and a 150 km thick air layer with a sticky air viscosity of 10^{19} Pa s. The buoyant mantle plume , with~~ , considering a buoyant plume (radius 100 km, ~~has a density of~~ density 3,200 kg m^{-3}; 100 kg m^{-3} less than ~~that of~~ the surrounding mantle and lithosphere~~. 100 tracers per cell are used for advecting material properties and for tracking the location of the surface in the case of the marker-in-cell method. Acceleration due to gravity g is set to 10 m s^{-2}~~) rising through a 2800 × 850 km domain at 1024 × 256 resolution over 20 My. The sticky air layer has a viscosity of 10^{19} Pa s. Free slip boundary conditions are imposed at the horizontal edges and top of the model, while a no-slip boundary condition is imposed at the bottom~~boundary, and a free slip condition is imposed at the top. The model is run for 20 My, which allows for the plume to rise through the mantle and impinge upon the lithosphere causing deformation of the surface~~. All other parameters follow Crameri et al. (2012a).

Analytical solutions for this benchmark are not available. However, results from multiple numerical geodynamic models, including finite element models with true deformable free surfaces, were run as part of the study of Crameri et al. (2012a) and consistently show a maximum surface deformation ~~800-850~~ 800–850 km after 20 My.

The results of the plume benchmark further demonstrate the strengths of Lagrangian tracking methods in isolating the topographic response of the model without the noise associated with the marker-in-cell method. The marker-in-cell method introduces random noise, which results in a ≈100 m discrepancy in topography at the centre of the plume. Lagrangian tracking methods closely matched the results demonstrated by Crameri et al. (2012a) for both the maximum topography at 20 My and the evolution of topography in the intervening time.

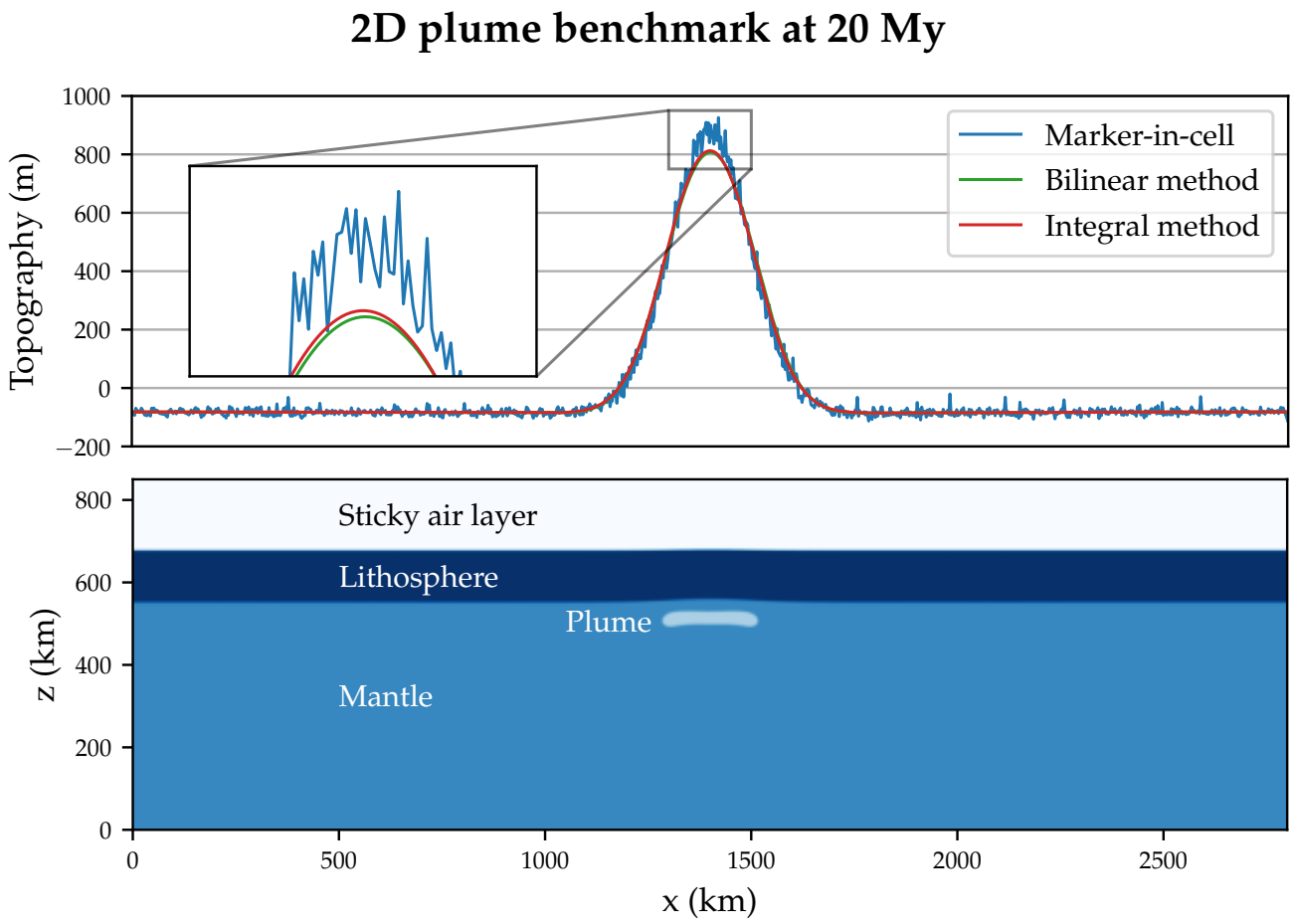

Figure 16. After 20 My all methods produce results similar to those demonstrated in Crameri et al. (2012a)~~, however, the~~ . The marker-in-cell ~~and integral~~ method ~~demonstrate~~ demonstrates significantly more noise compared to the ~~other~~ Lagrangian methods and a systematically raised maximum topography.

5.3 2D scaling tests

Scaling tests ~~in 2D were performed using~~ used a non-dimensional model in spherical ~~geometry, an example of which is shown in Figure A1. The model setup involves a constant viscosity mantle with Rayleigh number Ra $= 10^7$, and a sticky air layer with a thickness 10% that of the mantle with a viscosity contrast $\eta_{\text{rock}}/\eta_{\text{air}} = 10^3$. All scaling models were run for a total of~~ annulus geometry with constant viscosity (Ra $= 10^7$), run for 5,000 ~~time steps to ensure that a statistically steady state convection was reached.~~

~~Two tests were performed to judge the performance of the methods in 2D: tests of different surface marker densities, and tests of different model resolutions. In both cases, the amount of computational effort spent tracking surfaces using Lagrangian~~

markers can be divided into four main operations: advection (including sorting of the marker chain), interpolation, smoothing, and unmixing. The relative impact of these four operations can be compared to judge the efficiency of the bilinear and integral methods.

Example of topography generated using a simple constant viscosity model in 2D spherical geometry. The underlying temperature field shows the location of various plumes and downwellings, which are captured in the surface topography generated using the bilinear method. This model forms the basis of the 2D scaling tests performed.

5.3.1 2D scaling with surface marker density

The first scaling test examines the effect of marker density on performance. Marker densities ranging from 1 marker per cell (MPC) to 64 MPC were tested, with performance evaluated for both the bilinear and integral methods(Figure 17). The computational time needed for the surface tracking method is expressed as a fraction of the total computational time, which also includes calculating the Stokes solution using the MUMPS direct solver (accessed via PETSc), advecting the temperature field using a TVD method, and advecting the volumetric tracers (as discussed earlier).

2D scaling test evaluating the impact of surface marker density (MPC) on tracking performance. The integral method demands more computational effort than the bilinear method, reaching a maximum of 11% of total computational effort at 64 MPC compared to 3% for the bilinear method. Tracer unmixing accounts for the majority of computational cost.

The results indicate that the bilinear method 's impact on total runtime is minimal, consistently accounting timesteps to ensure statistically steady-state convection (Figure **??**). Figure 17 shows performance as a function of surface marker density for both methods. The bilinear method consistently accounts for approximately 3% of computational effort total runtime across all tested MPC values. Conversely, , while the integral method exhibits a significant increase in computational demand as marker density increases, peaking peaks at 11% of total runtime at 64 MPC.

The unmixingoperation's inefficiency can be attributed to its requirement to loop through all tracers In both cases the dominant cost is marker unmixing, which requires looping through all markers in the model to determine their position relative to the surface. This process alone accounts for approximately 2–3% of total runtime, as observed in the bilinear method. Additional computational effort is incurred when determining the surface location using linear interpolation and identifying a suitable template for the tracer exchange method. For the bilinear method, determining the surface location at a given point can be performed in constant : a procedure taking $O(1)$ time , whereas the integral method requires $O(\log n)$ time.

Other operations, such as advection and interpolation, impose minimal computational overhead in both methods. However, sorting, an operation unique to the integral method, scales with the number of surface markers per cell (MPC). This increased cost is primarily due to the requirement for additional iterations of the slope limiting algorithm at higher marker densities.

5.3.1 2D scaling with resolution

The second scaling test involves investigating the effect of changing resolution. Four model resolutions were tested: 128×16, 256×32, 512×64, and 1024×128, and the model performance measured per marker for the bilinear and integral method at each resolution. For each resolution, model performance was assessed using both the bilinear and integral methods. A fixed

~~marker~~ method but $O(\log n)$ for the integral method. Tests across four resolutions (128×16 to 1024×128) at a fixed density of 8 ~~surface markers per cell (MPC) was maintained throughout all tests.~~

~~Scaling test in 2D investigating the effect of resolution on surface tracking performance as a percentage of total computational effort. Tracer unmixing dominates runtime for both methods, a result of unmixing being dependent on tracer density instead of surface marker density.~~

~~The results reveal that while the computational effort required for advection, interpolation, and smoothing decreases (as a fraction of total computational effort) with increasing resolution, the effort required for unmixing scales proportionally with resolution. This behaviour arises because the unmixing process depends on the number of tracers in the model, which increases with resolution. Due to the increased computational overhead of determining surface position for each for these tracers when using the integral method,~~ MPC confirm this pattern: unmixing scales with marker count rather than surface marker count, leaving the bilinear method ~~performs better overall, consistently taking less than~~ below 3% of ~~the overall runtime~~ total runtime at all resolutions tested.

5.4 ~~3D benchmark summary~~

~~Similarly to~~

5.4 3D plume benchmark

The 2D plume benchmark ~~presented in Section 5.2 can be extended into 3D. The domain in~~ was extended to 3D ~~is~~ on a $1400 \times 1400 \times 850$ km Cartesian ~~box with a resolution of~~ domain at $256 \times 256 \times 64$ ~~, a resolutionchosen to balance the high computational cost of 3D models with accuracy. The model consists of a 600 km thick mantle, a 100 km thick lithosphere, and a 150 km thick air layer. The geometry of the mantle plume is~~ resolution, with the plume geometry modified to a sphere ~~with an initial diameter of~~ of initial diameter 100 km. A ~~rigid (no slip)~~ no-slip boundary condition is imposed at the lower boundary, while free slip ~~boundary condition is~~ conditions are imposed on all other boundaries. All other physical parameters ~~remain identical between~~ are identical to the 2D ~~and 3D models. As this 3D version is a novel benchmark, there are no previous results available for comparison~~case. As no prior 3D results exist for comparison, results are assessed qualitatively.

~~3D plume benchmark setup, the 3D extension of the 2D plume benchmark above and in Crameri et al. (2012a). 3D models are run at a resolution of $256 \times 256 \times 64$~~

The performance of different tracking methods, as illustrated in Figure 18, highlights the inherent noise challenges of the marker-in-cell method in 3D. This method struggles with noise generation due to the inherent dependence on ~~tracer~~ marker density and positioning. Nonetheless, it is still able to capture the main features of the mantle plume, particularly the central topographic uplift created by the buoyant upwelling. ~~The~~ Both the bilinear and integral methods ~~, although somewhat effective at reducing~~ eliminate this noise, ~~still display disturbances across varying spatial scales, emphasizing the need for improved coupling techniques.~~

~~3D plume benchmark topography at 20 My (top-down view). The marker-in-cell method with 100 tracers per cell is able to capture the subtle topography generated by the mantle plume at the centre of the model, however noise inherent in this method~~

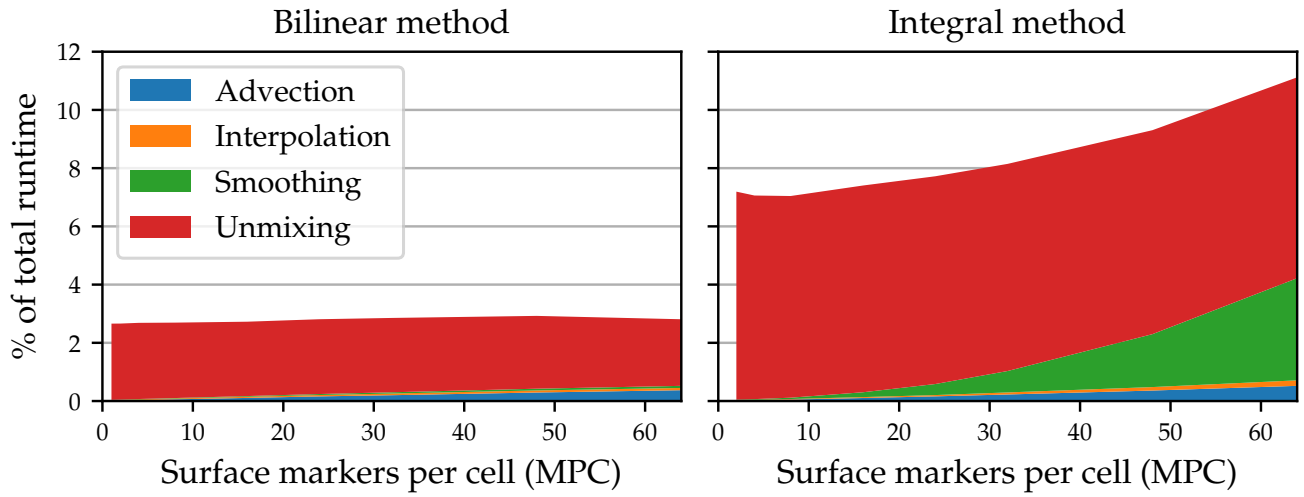

Figure 17. 2D ~~, it is possible to run a set of benchmarks to test the efficiency and accuracy of Lagrangian surface tracking in 3D. The combinations of parameters used for models in 3D are summarised in Table 2. Unless otherwise stated, all 3D models presented below use these combinations of parameters.~~

~~Summary of Lagrangian surface tracking options used in 3D benchmarks **Method Surface MPC Reinitialisation Smoothing method Unmixing method** Marker-in-cell - - - bouncing Bilinear method 16 global reinitialisation after each timestep - bouncing Integral method 16 interval method $\Delta x/\Delta x_{\text{init}} \in [0.2, 3.0]$ slope limiter $s_{\text{crit}} = 0.5$ exchanging~~

~~A summary of the 3D benchmarks run can be found in Table **??**.~~

~~Summary~~ scaling test evaluating the impact of ~~Lagrangian~~ surface marker density (MPC) on tracking ~~benchmarks~~ performance. The integral method demands more computational effort than the bilinear method, reaching a maximum of 11% of total computational effort at 64 MPC compared to 3% for the bilinear method. Marker unmixing accounts for the majority of computational cost in ~~3D~~both methods.

~~**Benchmark Geometry Resolution Description** 3D plume Cartesian $256 \times 256 \times 128$ Dynamic topography resulting from a rising mantle plume 3D constant viscosity Cartesian Various Constant viscosity models with $\text{Ra} = 10^7$ used for comparison with the marker-in-cell method and for investigating performance scaling with different surface marker densities and resolutions~~

~~is visually apparent. Both the bilinear and integral method eliminate this noise, providing visually similar results that isolate the plume's influence on topography.~~

~~Figure 19 further emphasizes these findings by providing a cross-sectional view through the model. The marker-in-cell method's pronounced noise is visually prominent in the profile, while the integral and bilinear methods show considerable improvement. Minor~~ providing visually similar results that isolate the plume's influence on topography, with minor differences between the two methods ~~are visible~~ visible in the cross-sectional profile (Figure 19), possibly a side effect of the differing smoothing methods used.

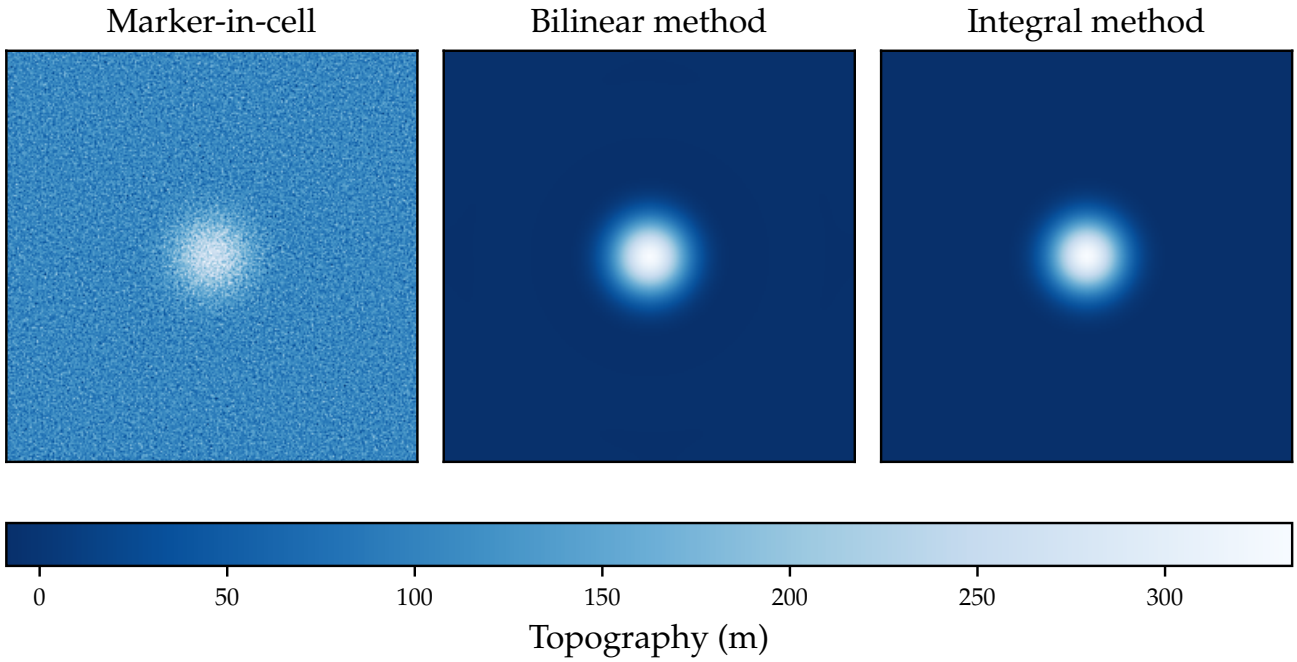

Figure 18. 3D plume benchmark topography at 20 My (top-down view). The marker-in-cell method with 100 markers per cell captures the topography generated by the mantle plume but with visually apparent noise. Both the bilinear and integral methods eliminate this noise.

5.5 3D constant-viscosity Cartesian ~~box~~convection

~~As a comparison to the models shown in Figure ??, a~~ A simple Cartesian box setup (Figure 20) with a relatively coarse $64 \times 64 \times 32$ resolution was used ~~as a basis for testing various aspects of the surface tracking methods . This model considers convection with a constant viscosity using~~ to compare the three methods under constant-viscosity convection with non-dimensional parameters ~~with~~ (Ra $= 10^7$~~. The topography generated by the five methods can be compared against the topography generated by a high-resolution marker-in-cell method to compare accuracy.~~

~~Surface topography as generated by three methods at 100 markers per cell. The marker-in-cell method is the baseline (see also Figure ??). Both Lagrangian tracking methods provide visually smoother topography.~~

~~The noise inherent with the marker-in-cell method is shown by its wide distribution of topography.~~

~~).~~ Visual inspection of ~~the results in Figure 21 show~~ Figure 21 confirms that both the ~~Bilinear and Integral method are able to eliminate the~~ bilinear and integral methods eliminate the marker-density-dependent noise of the marker-in-cell method~~and isolate the plume topography~~, producing visually smooth topography that isolates the underlying plume and downwelling structure.

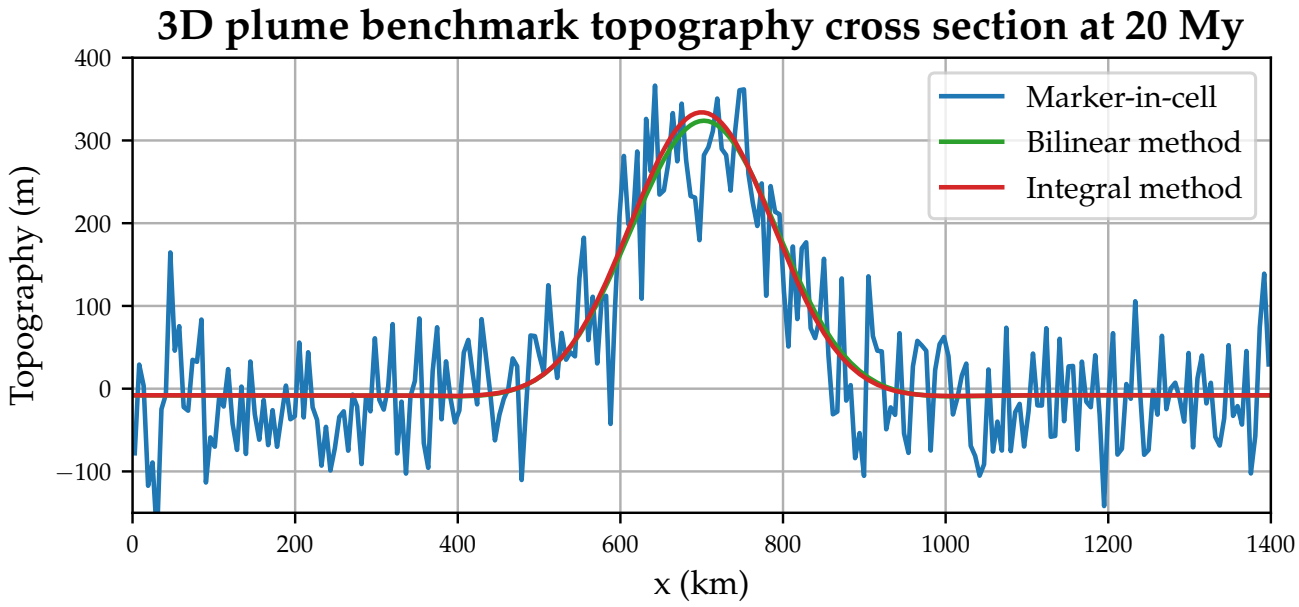

Figure 19. 3D plume benchmark topography at 20 My ~~by surface tracking method~~ (cross section). ~~Similar to the corresponding 2D benchmark, both~~ Both the bilinear and integral methods ~~are able to~~ effectively capture topography without the noise inherent in the marker-in-cell method. Minor differences between the two Lagrangian methods are visible, likely a consequence of the differing smoothing approaches.

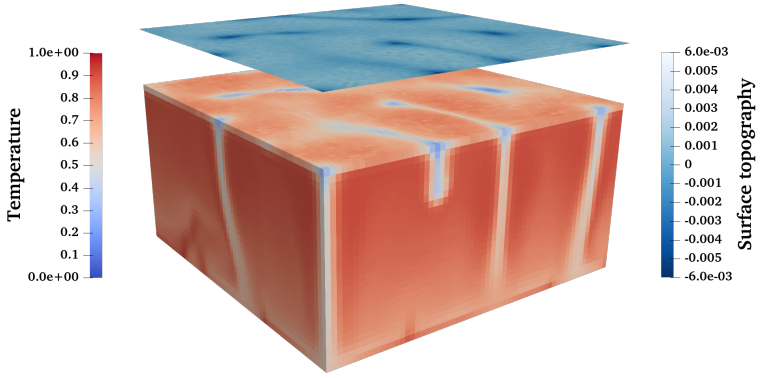

Figure 20. A nondimensional constant-viscosity Cartesian box test model ($\mathrm{Ra} = 10^7$). A sticky air discretisation with a viscosity contrast of $\eta_{\mathrm{air}}/\eta_{\mathrm{rock}} = 10^{-3}$ is used. A relatively coarse resolution of $64 \times 64 \times 32$ is used to better highlight the effect of low volumetric marker densities on topography.

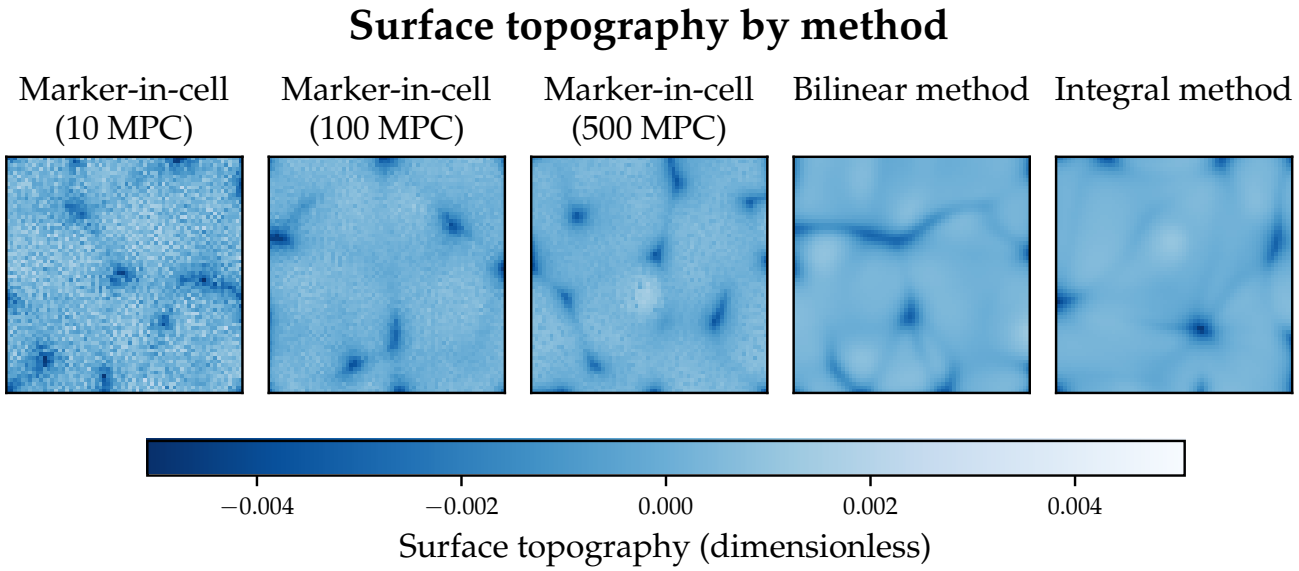

Figure 21. Surface topography generated by the marker-in-cell method at various marker densities, compared against the bilinear and integral Lagrangian tracking methods at a density of 100 markers per cell. Both Lagrangian approaches yield smoother topography, achieving a quality comparable or exceeding the high-density marker-in-cell results.

5.6 3D scaling tests

The same Cartesian box model was used ~~in order~~ to test scaling of surface tracking methods with respect to ~~three variables: model resolution , tracer density and surface~~ model resolution and marker density.

5.6.1 Resolution dependence~~test~~

The resolution dependence test ~~involved the simple Cartesian box model evaluated~~ evaluated the model at four resolutions ~~,~~ ranging from $32 \times 32 \times 16$ to $256 \times 256 \times 128$~~, while keeping all other parameters constant.~~

~~To qualitatively assess the impact of resolution, a top-down view of the surface topography at the final timestep, as tracked using the integral method, is shown in Figure 22~~ .

~~3D surface topography tracked using the integral method at different resolutions. The smooth topography is consistent across length scales. Higher resolutions resolve greater detail smoothly, while lower resolutions produce more diffuse, but still smooth, features in downwelling regions. Similar results can be obtained when using the bilinear method.~~

~~The results of this qualitative test indicate that the smooth topography achieved using the integral method is consistent~~ Figure 22 shows that smooth topography is achieved consistently across all length scales using the integral method, in contrast to the grainy ~~and unrefined~~ topography produced by the marker-in-cell method~~. Similar results were observed for~~ ; similar results are

obtained with the bilinear method. As expected, higher resolutions reveal Higher resolutions resolve greater detail, particularly around regions near downwellings, while these features appear more diffuse at lower resolutions .

To quantitatively analyse the effects of varying resolutions, the time-averaged surface topography distributions were examined. Variable resolutions pose a challenge for comparison because the timesteps and total runtime differ due to the constant CFL number maintained across all resolutions. At higher resolutions, velocities are more constrained, resulting in longer simulation times. For example, the lowest resolution ($32 \times 32 \times 16$) achieved a final model time approximately 7.3 times greater than the highest resolution ($256 \times 256 \times 128$) after 5000 timesteps. To account for this, only overlapping time intervals were analysed, excluding the initial timesteps to allow for the establishment of a steady-state convective regime. The results are shown in Figure **??**.

Time averaged topography distributions for a variety of resolutions using the integral method (corrected for variable model runtimes). A general trend towards increased median topography with resolution is seen, which is the expected result of a diffuse representation of trenches at lower resolutions.

The analysis indicates a clear dependence on model resolutionlower resolutions produce more diffuse but still smooth features. The median topography increases with higher resolutions, resolution while the mean topography remains consistently remains at 0.0. This pattern suggests the presence of deeper trenches , consistent with deeper trenches being better resolved at higher resolutionsthat skew the median. This result aligns with expectations, as higher resolutions better resolve trench features, which appear more diffuse at lower resolutions. Notably, these observations could not have been achieved with . This resolution dependence can only be observed using the Lagrangian tracking methods, as the marker-in-cell methods, which are heavily influenced by both tracer density and model resolutionresults are dominated by marker-density-dependent noise at equivalent marker counts.

The performance of each method was also evaluated at different resolutions , as is shown in Figure 23. Similar to the As in 2Dscaling tests, the performance of both methodsis dominated by the unmixing operation. Unmixing scales with the number of tracers rather than the number of surface markers, marker unmixing dominates runtime for both methods. For the bilinear method, determining surface location at a given location can be accomplished in constant surface location lookups are $O(1)$time, while the integral method requires iterating through Delaunay triangles, which scales with , keeping unmixing cost roughly constant across resolutions. For the integral method, the $O(\log n)$ (where n is the number of surface markers) in the best case. Consequently, unmixing time remains roughly constant for the bilinear method across resolutions, whereas it generally increases with resolution for the integral method. For 3D models, the use of iterative solvers introduces some variability to the overall solution time, accounting for the variation in timing results observed.

Other components, such as advection and interpolation, require minimal computational effort for both methods across all resolutions. However, the integral method's lookup cost means unmixing generally increases with resolution. The slope limiting algorithm for marker mesh smoothing adds significant computational cost to that method, which scales adds further cost to the integral method, scaling with resolution due to the increased iterations required to relax the marker meshat higher resolutions.

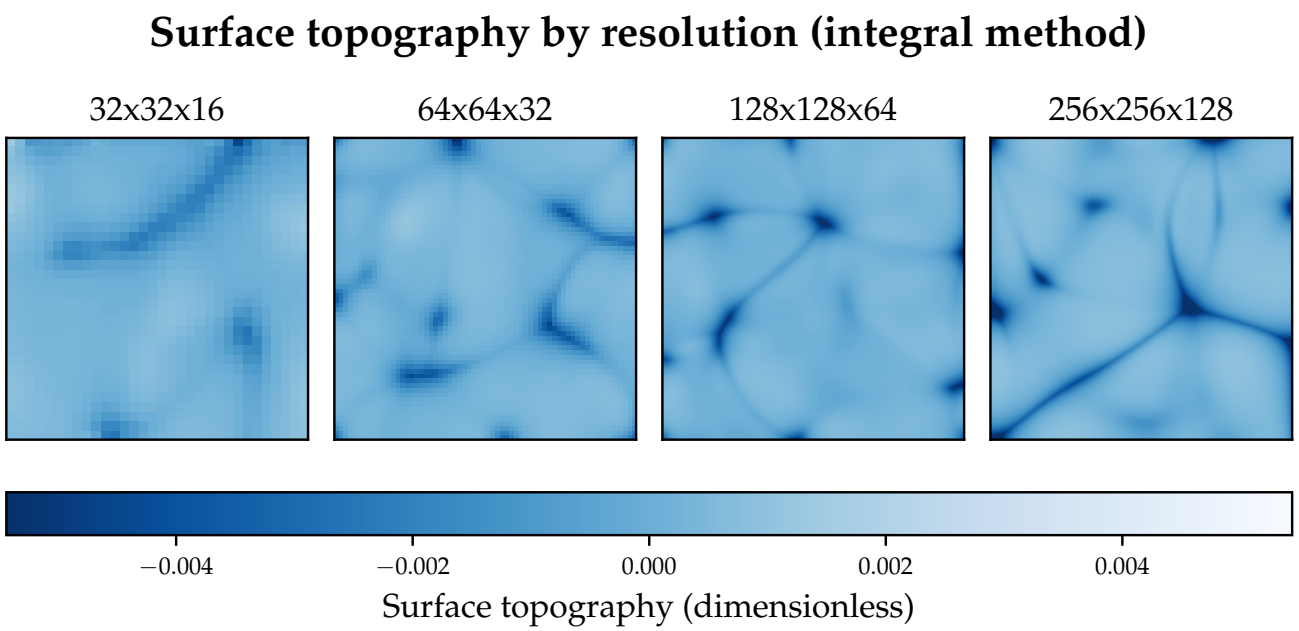

Figure 22. 3D surface topography tracked using the integral method at different resolutions. Smooth topography is consistent across length scales, with higher resolutions resolving greater detail around downwelling regions. Similar results are obtained with the bilinear method.

5.6.2 ~~Tracer~~ Marker density dependence~~test~~

A key question is whether the implemented methods ~~can~~ eliminate the dependence on ~~tracer density and the associated reduction in computation performance that comes with it, as discussed in Section ??. This can be tested by running a series of models with varying tracer densities and comparing their surface topography (Figure 24) to determine both qualitatively and quantitatively whether there is a persistent dependence on tracer density.~~

~~Surface topography as determined using the integral method by tracer density. No qualitative differences are seen in the surface topography reconstruction when changing the underlying tracer density. A similar result can be seen for the bilinear method.~~

~~The smooth surface topography demonstrates that there is no longer any dependence of surface topography on tracer density, in contrast to the~~ volumetric marker density discussed in the introduction. Figure 24 shows surface topography produced by the integral method across a range of volumetric marker densities: no qualitative differences are visible, in stark contrast to marker-in-cell ~~method, which is as expected because the density and viscosity values near the surface are adjusted directly from the tracked surface position. This is a positive result, as it implies~~ results. The same result is obtained with the bilinear method. This confirms that model performance can be improved by ~~decreasing tracer~~ reducing marker density without compromising ~~the quality of the surface topography. These results were also verified by comparing time-averaged topographic distributions.~~

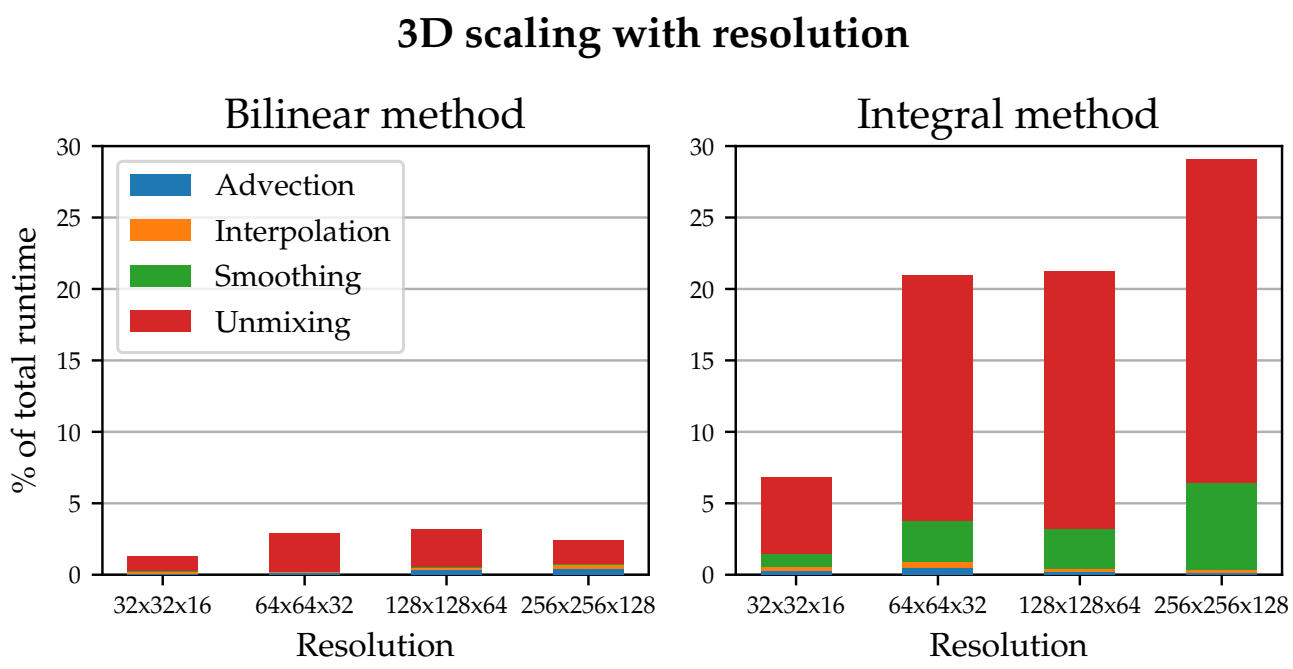

Figure 23. Performance of each method with resolution as a percentage of total runtime. The bilinear method performs significantly better than the integral method in 3D, ~~particularly in terms of tracer~~ with marker unmixing ~~, which was the biggest contributor to~~ the ~~performance of~~ dominant cost in both ~~methods~~cases.

5.6.3 ~~Surface marker density dependence test~~

~~A final question to answer through scaling tests is the dependence of the methods on the density of the surface markers themselves. All other models in 3D were run using a surface marker marker density of $4 \times 4 = 16$ markers per cell, however this was chosen arbitrarily. In order to test the surface marker density dependence, scaling tests were performed for marker densities corresponding to all square numbers betwen $1 = 1 \times 1$ markers per cell, and $64 = 8 \times 8$ markers per cell on a constant viscosity $64 \times 64 \times 32$ Cartesian box domain. First, the performance of different surface marker densities was considered for both the integral and bilinear methods, as shown in Figure ??~~topographic quality, since the density and viscosity fields near the surface are determined directly from the tracked surface position rather than from the marker distribution.

~~As expected based on previous results~~

6 Summary and discussion

6.1 Summary of key results

~~Smoothing and unmixing take up the majority of~~

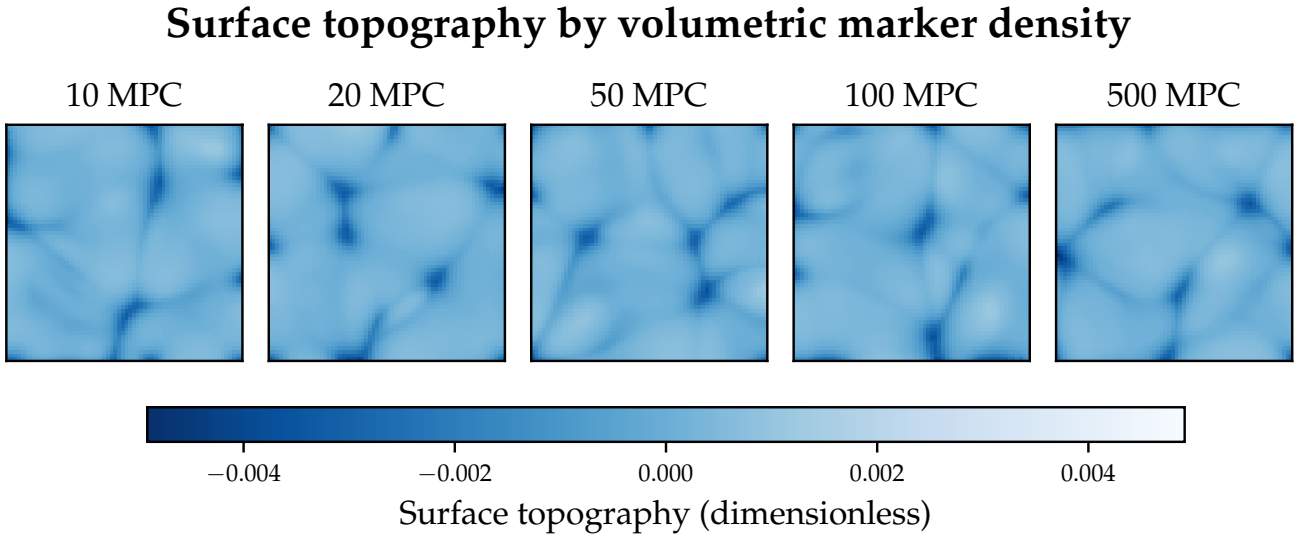

Figure 24. Surface topography as determined using the ~~runtime in 3D models, especially at high marker~~ integral method with varying markers per cell~~counts~~. No qualitative differences are seen in surface topography reconstruction. A similar result is obtained for the bilinear method.

This study implemented and benchmarked two Lagrangian surface marker tracking methods, the bilinear method ~~consistently outperforms~~ and the integral method~~across all MPC counts. Unmixing dominates computational effort for the same reasons discussed previously: for the integral method, unmixing depends not only on tracer density but on the number of surface markers, requiring $O(\log n)$ time to determine surface height at a given location.~~

7 ~~Summary and discussion~~

6.1 ~~Summary of key results~~

~~The key results of this study can be summarised with several points, which are elaborated upon in the discussion below:~~

~~Lagrangian surface markers are a simple and effective way of tracking free surfaces in numerical geodynamic models.~~ , in the mantle convection code StagYY, comparing them against the existing marker-in-cell approach. Both new methods produce high-resolution, low-noise surface topography that is independent of volumetric marker density, unlike the marker-in-cell method, allowing significant reductions in volumetric marker count and associated computational cost. The bilinear method ~~is able to track surfaces accurately and with good performance, however it does introduce~~ offers the best computational performance, consistently accounting for less than 3% of total runtime, and is straightforward to implement, though it introduces some artificial numerical diffusion due to periodic global reinitialisation. The integral method ~~is also able to track surfaces accurately, however it requires additional methods to smooth and stabilise the surface, and is significantly less performant~~

~~than the bilinear method.~~ produces topography of comparable quality but at greater computational cost, due primarily to the $O(\log n)$ surface lookups required during marker unmixing and the overhead of slope limiting. Both methods can be used to obtain volume fractions for coupling the ~~location of the surface to the underlying Stokes solver through the~~ surface location to the density and viscosity fields used by the Stokes solver (ρ, η ~~coupling). Coupling of the surface tracking method to the underlying Stokes solver through ρ, η~~ coupling~~is~~), and this coupling is found to be essential for smooth and accurate surface tracking results. ~~When tracking topography, performance gains are possible by reducing tracer density without sacrificing topographic quality due to the independence of the reconstructed surface on tracer density .~~

6.1 Discussion of key results

6.1.1 Novelty and relation to prior work

The bilinear method presented here is not entirely new: a closely related approach is already used in the regional-scale code LaMEM (Kaus et al., 2016), and a simplified 2D version was employed by Duretz et al. (2016) to test free surface discretisation methods. A related approach using a Delaunay-triangulated surface embedded in an Eulerian mesh was previously implemented in the code DOUAR (Braun et al., 2008). The novelty of this study lies in the extension and thorough benchmarking of both methods to 3D spherical geometry within StagYY, the development of the slope-limiting stabilisation algorithm for the integral method, the introduction of ρ, η coupling to the Stokes solver, and the demonstration that volumetric marker density can be substantially reduced without loss of topographic accuracy.

6.1.2 Implementation

The implementation of Lagrangian surface markers, especially the bilinear method, is relatively straightforward. Since Lagrangian ~~tracers~~ markers already exist in StagYY, as they do for many other numerical geodynamic modelling codes, existing routines for manipulating these ~~tracers~~ markers were easily adapted for the new surface markers. Reconstructing the surface using the bilinear representation was similarly straightforward and could likely be implemented in other numerical geodynamic codes with minimal effort. ~~Indeed, a variation of the bilinear method described here is already integrated into the geodynamic code LaMEM (Kaus et al., 2016), and a simplified 2D version was employed by Duretz et al. (2016) to test free surface discretisation methods.~~

In contrast, the integral method is significantly more complex to implement, particularly due to the need for surface marker reinitialisation and smoothing. The 3D implementation requires a significant amount of code for performing complex operations, such as computing the Delaunay triangulation and determining cellwise volume fractions. Developers considering these methods should carefully weigh the cost-benefit trade-offs, especially given the integral method's performance limitations ~~,~~ ~~which are discussed further~~ discussed below.

6.1.3 Bilinear method

The bilinear method was able to produce high-resolution topography ~~,~~ and demonstrated the best computational performance among the methods tested.

~~The primary strength of the bilinear method lies in its computational efficiency.~~ Key surface marker ~~chain/mesh~~ operations, such as marker advection and surface reconstruction, are performed in linear time $O(n)$ with respect to the number of surface markers. Once surface locations are interpolated to nodes, determining the surface height at a specific point can be achieved in constant time $O(1)$~~. This efficiency~~ , which significantly benefits operations ~~that require frequent lookups of surface heights~~requiring frequent surface height lookups, such as ~~the tracer unmixingoperation~~marker unmixing.

Global reinitialisation introduces implicit numerical diffusion ~~, which helps stabilise~~ that stabilises the marker chain and avoids the need for explicit smoothing~~operations~~, improving performance. However, this ~~same~~ diffusion can gradually reduce the accuracy of the surface representation~~. While some diffusion is necessary to maintain stability and prevent marker entrainment, it can potentially come~~ , potentially at the cost of precision when considering sub-grid scale features.

6.1.4 Integral method

The integral method can produce similarly high-quality topography to the bilinear method but is less performant.

Its main advantage is the absence of artificial numerical diffusion, as surface markers move independently of the Eulerian grid and are only adjusted where needed. In 3D, Delaunay triangulation offers a natural surface representation ~~,~~ suitable for visualising fine-scale features, tracking sea level, and potentially integrating surface process models. However, the method's reliance on several $O(n \log n)$ operations such as marker sorting and reinitialisation limits its efficiency~~. Although advection and reconstruction remain $O(n)$,~~ , and slope limiting adds further cost ~~and~~ that cannot be solved in linear time. The largest performance bottleneck in both 2D and 3D is ~~tracer unmixing. Unlike the constant-time interpolation of the bilinear method, the integral method requires $O(n \log n)$ per tracer~~marker unmixing, which requires $O(\log n)$ per marker, leading to $O(m \log n)$ overall with m ~~tracers~~markers. This cost remains significant even after optimisation of the unmixing algorithm~~to reduce the number of tracers that are subjected to the unmixing operation~~.

6.1.5 Comparison ~~of implemented methods~~ with the marker-in-cell method

Both ~~the~~ implemented methods improve upon the existing marker-in-cell method in ~~several ways~~two key respects. Firstly, ~~it bypasses~~ they bypass the need for ~~a high tracer density~~ high volumetric marker densities to obtain high-quality surface topography, ~~and therefore allows~~ allowing for significantly decreased computational effort and memory consumption~~, with the tradeoff of higher computational effort required for the surface tracking methods themselves~~. Secondly, the implemented methods are more accurate~~than marker-in-cell based methods~~, reducing topographic noise on all scales~~and allowing the accurate modelling of surface topography~~. The trade-off is a modest increase in computational effort for the surface tracking operations themselves, which in all tests remained well below the cost of volumetric marker advection at the densities required by the marker-in-cell method.

6.1.6 Necessity of density and viscosity coupling

A key result of this study is the necessity of coupling the location of the surface to the underlying physical model through the density and viscosity fields, referred to as ρ, η coupling in Section 4.2. This coupling is essential to avoid topographic noise that arises ~~as a result of~~ from determining density and viscosity based on a finite number ~~discrete tracers~~ of discrete markers with a random initial distribution.

The requirement for ~~coupling density directly to the surface~~ density coupling was also noted ~~in the results of Duretz et al. (2016) , in which a conceptually similar method to the ρ, η coupling used here was applied. However,~~ by Duretz et al. (2016); the methods presented here ~~take~~ extend this further with application to the viscosity field as well.

6.2 Applications and future directions

6.2.1 Surface processes

A potential future research direction would be the ~~implementation of more sophisticated smoothing methods, or even the~~ direct implementation of surface processes into StagYY. While the diffusion and slope limiting methods presented here can be considered ~~to be very simple methods of modelling~~ very simple representations of erosion and sedimentation, a direct representation of the surface ~~that is~~ coupled to the underlying model theoretically allows for fully coupled modelling of surface processes on the global scale for the first time.

~~Potential future research directions might~~ Prior work coupling geodynamic codes to surface process models has been carried out at regional scales (e.g. (Simpson, 2004; Burov and Toussaint, 2007; Braun, 2010; Bahadori et al., 2022; Wolf et al., 2025)), but global-scale coupling remains an open problem. A natural direction would be the incorporation of a surface process model such as Badlands (Salles, 2016) directly into StagYY~~which could modify~~ , modifying the surface at each timestep ~~. With the coupling of the free surface to~~ in a way that feeds back into the underlying model through ~~tracer unmixing and coupling to the Stokes solver, this modified surface would then have a direct effect on the underlying model. This presents an opportunity for future research to incorporate both surface processes and a free surface boundary condition together on the global scale~~the existing marker unmixing and ρ, η coupling machinery.

6.2.2 Alternative Stokes solvers

~~A surface tracking method must be coupled with an appropriate solver in order to fully solve the free surface problem.~~ While the results presented ~~in this chapter~~ here have all employed the sticky air method to approximate the ~~solution to the free surface problem, other methods of modelling free surfaces exist that can be coupled with Lagrangian surface tracking to form a complete free surface solver.~~

~~One such method is the staircase representation of the surface presented by Duretz et al. (2016) . In this method, no equations are solved within the air layer, and~~ free surface boundary condition, the direct surface representation is compatible with alternative solvers. The staircase discretisation of Duretz et al. (2016) eliminates the need for a sticky air layer entirely by

applying alternative boundary conditions ~~are applied~~ to cells near the surface~~in order to approximate a free surface solution without the need for a sticky air layer. A prerequisite of this method is~~ , requiring only a method to determine whether ~~the midpoint of a given cell is~~ a cell centre lies above or below the surface, which is readily ~~achieved using~~ provided by a marker chain or mesh.

~~The direct representation of the surface also enables the possibility of implementing the~~ The variational Stokes discretisation ~~presented in Larionov et al. (2017). The key requirements for the implementation of this method are~~ of Larionov et al. (2017) is also compatible, requiring volume fraction functions ~~, which were already implemented~~ that are already computed as part of the ~~coupling method~~ ρ, η coupling described in Section 4.2.

6.2.3 Sea level modelling

Accurately tracking the evolution of sea levels over time is a key capability of the direct surface tracking methods presented here~~and has several promising applications.~~

~~.~~ Sea level tracking is a necessary step toward coupling geodynamic models with climate and biological evolution models~~. Climate~~ : climate models such as FOAM (Tobis et al., 1997) and biological models like Gen3sis (Hagen et al., 2021) require information about continental configurations ~~, which~~ that can be more accurately provided by dynamically computing sea level changes from an initial ocean volume.

~~Through direct and accurate surface tracking, the evolution of a constant sea volume can be tracked to give information about changes in sea level and coverage area.~~ As StagYY already includes functionality to estimate volatile outgassing rates ~~,~~ including water, it would theoretically be possible to incorporate ~~this into a model which considers~~ a changing sea volume ~~. This would enable for the first time to couple surface processes with interior processes in such a way to allow for~~ into the model, enabling more integrated models linking deep Earth dynamics with climate, landscape, and biosphere evolution.

Code availability. The code StagYYFS, a testbed code based on StagYY, may be used to produce the benchmark results and figures used in this paper. It is archived on Zenodo under the GPLv3 license under https://doi.org/10.5281/zenodo.18096249 (Tackley and Gray, 2025).

Appendix A: Spherical annulus benchmark

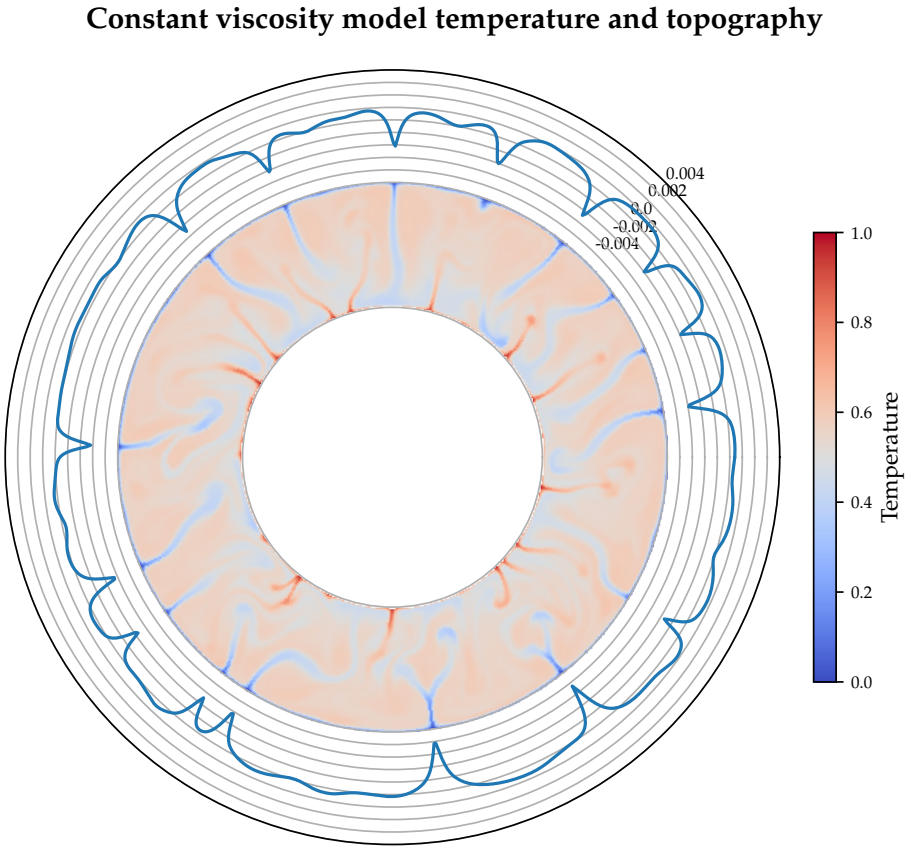

Figure A1. Example of topography generated using a simple constant viscosity model in 2D spherical geometry. The underlying temperature field shows the location of various plumes and downwellings, which are captured in the surface topography generated using the bilinear method. This model forms the basis of the 2D scaling tests performed.

Author contributions. **Timothy Gray**: original study design; code and algorithm development; scaling and performance benchmarks; figure creation. **Paul Tackley**: development of StagYY; conceptual input; manuscript review and editing. **Taras Gerya**: conceptual input; manuscript review.

Competing interests. The authors declare that they have no conflict of interest.

Acknowledgements. This work was supported by Swiss National Science Foundation #192296. We thank the two anonymous reviewers for constructive reviews that improved this manuscript.

References

Bahadori, A., Holt, W. E., Feng, R., Austermann, J., Loughney, K. M., Salles, T., Moresi, L., Beucher, R., Lu, N., Flesch, L. M., Calvelage, C. M., Rasbury, E. T., Davis, D. M., Potochnik, A. R., Ward, W. B., Hatton, K., Haq, S. S. B., Smiley, T. M., Wooton, K. M., and Badgley, C.: Coupled influence of tectonics, climate, and surface processes on landscape evolution in southwestern North America, Nat Commun, 13, 4437, https://doi.org/10.1038/s41467-022-31903-2, 2022.

Braun, J.: The many surface expressions of mantle dynamics, Nature Geoscience, 3, 825–833, https://doi.org/10.1038/ngeo1020, bandiera_abtest: a Cg_type: Nature Research Journals Number: 12 Primary_atype: Reviews Publisher: Nature Publishing Group Subject_term: Geodynamics;Geomorphology;Structural geology;Tectonics Subject_term_id: geodynamics;geomorphology;structural-geology;tectonics, 2010.

Braun, J., Thieulot, C., Fullsack, P., DeKool, M., Beaumont, C., and Huismans, R.: DOUAR: A new three-dimensional creeping flow numerical model for the solution of geological problems, Physics of the Earth and Planetary Interiors, 171, 76–91, https://doi.org/https://doi.org/10.1016/j.pepi.2008.05.003, recent Advances in Computational Geodynamics: Theory, Numerics and Applications, 2008.

Burov, E. and Toussaint, G.: Surface processes and tectonics: Forcing of continental subduction and deep processes, Global and Planetary Change, 58, 141–164, http://www.sciencedirect.com/science/article/B6VF0-4NF4F5C-3/2/ce0b8a182ab52e3f36698cd0d56fcae6, 2007.

Coltice, N., Husson, L., Faccenna, C., and Arnould, M.: What drives tectonic plates?, Science Advances, 5, eaax4295, https://doi.org/10.1126/sciadv.aax4295, publisher: American Association for the Advancement of Science Section: Research Article, 2019.

Crameri, F., Schmeling, H., Golabek, G. J., Duretz, T., Orendt, R., Buiter, S. J. H., May, D. A., Kaus, B. J. P., Gerya, T. V., and Tackley, P. J.: A comparison of numerical surface topography calculations in geodynamic modelling: an evaluation of the 'sticky air' method, Geophysical Journal International, 189, 38–54, https://doi.org/10.1111/j.1365-246X.2012.05388.x, 2012a.

Crameri, F., Tackley, P. J., Meilick, I., Gerya, T. V., and Kaus, B. J. P.: A free plate surface and weak oceanic crust produce single-sided subduction on Earth, Geophysical Research Letters, 39, https://doi.org/10.1029/2011GL050046, _eprint: https://agupubs.onlinelibrary.wiley.com/doi/pdf/10.1029/2011GL050046, 2012b.

Duretz, T., May, D., and Yamato, P.: A free surface capturing discretization for the staggered grid finite difference scheme, Geophysical Journal International, 204, 1518–1530, https://doi.org/10.1093/gji/ggv526, 2016.

Gerya: Introduction to Numerical Geodynamic Modelling, Cambridge University Press, ISBN 978-1-107-14314-2, https://sfx.ethz.ch/sfx_lib4ri?url_ver=Z39.88-2004&ctx_ver=Z39.88-2004&ctx_enc=info:ofi/enc:UTF-8&rfr_id=info:sid/sfxit.com:opac_856&url_ctx_fmt=info:ofi/fmt:kev:mtx:ctx&sfx.ignore_date_threshold=1&rft.object_id=4930000000052441&svc_val_fmt=info:ofi/fmt:kev:mtx:sch_svc&, 2019.

Gerya, T., Duretz, T., and Rass, L.: New continuity-based velocity interpolation scheme for staggered grids, EGU General Assembly 2021, online, 19–30 Apr 2021, pp. EGU21–15 308, https://doi.org/10.5194/egusphere-egu21-15308, 2021.

Gerya, T. V. and Yuen, D. A.: Robust characteristics method for modelling multiphase visco-elasto-plastic thermo-mechanical problems, Physics of the Earth and Planetary Interiors, 163, 83–105, https://doi.org/10.1016/j.pepi.2007.04.015, 2007.

Gerya, T. V., Stern, R. J., Baes, M., Sobolev, S. V., and Whattam, S. A.: Plate tectonics on the Earth triggered by plume-induced subduction initiation, Nature, 527, 221–225, https://doi.org/10.1038/nature15752, bandiera_abtest: a Cg_type: Nature Research Journals Number: 7577 Primary_atype: Research Publisher: Nature Publishing Group Subject_term: Geodynamics;Tectonics Subject_term_id: geodynamics;tectonics, 2015.

Hagen, O., Flück, B., Fopp, F., Cabral, J. S., Hartig, F., Pontarp, M., Rangel, T. F., and Pellissier, L.: gen3sis: A general engine for eco-evolutionary simulations of the processes that shape Earth's biodiversity, PLOS Biology, 19, e3001 340, https://doi.org/10.1371/journal.pbio.3001340, publisher: Public Library of Science, 2021.

Joe, B.: GEOMPACK — a software package for the generation of meshes using geometric algorithms, Advances in Engineering Software and Workstations, 13, 325–331, https://doi.org/10.1016/0961-3552(91)90036-4, 1991.

Kaus, B. J., Popov, A. A., Baumann, T., Pusok, A., Bauville, A., Fernandez, N., and Collignon, M.: Forward and Inverse Modelling of Lithospheric Deformation on Geological Timescales Forward and Inverse Modelling of Lithospheric Deformation on Geological Timescales, in: Proceedings of nic symposium, vol. 48, pp. 978–983, John von Neumann Institute for Computing (NIC), NIC Series, https://juser.fz-juelich.de/record/507751/files/nic_2016_kaus.pdf, 2016.

Kreyszig, E.: Advanced Engineering Mathematics, John Wiley & Sons, ISBN 978-0-470-45836-5, google-Books-ID: UnN8DpXI74EC, 2010.

Larionov, E., Batty, C., and Bridson, R.: Variational stokes: a unified pressure-viscosity solver for accurate viscous liquids, ACM Transactions on Graphics, 36, 101:1–101:11, https://doi.org/10.1145/3072959.3073628, 2017.

Ogawa, M., Schubert, G., and Zebib, A.: Numerical simulations of three-dimensional thermal convection in a fluid with strongly temperature-dependent viscosity, Journal of Fluid Mechanics, 233, 299–328, https://doi.org/10.1017/S0022112091000496, 1991.

O'Rourke, J., Chien, C.-B., Olson, T., and Naddor, D.: A new linear algorithm for intersecting convex polygons, Computer Graphics and Image Processing, 19, 384–391, https://doi.org/10.1016/0146-664X(82)90023-5, 1982.

Patankar, S. V.: Numerical Heat Transfer and Fluid Flow, Hemisphere Publishing Corporation, New York, 1980.

Phongthanapanich, S. and Dechaumphai, P.: Adaptive Delaunay triangulation with object-oriented programming for crack propagation analysis, Finite Elements in Analysis and Design, 40, 1753–1771, https://doi.org/10.1016/j.finel.2004.01.002, 2004.

Ramberg, H.: Gravity, Deformation, and the Earth's Crust: In Theory, Experiments, and Geological Application, Academic Press, ISBN 978-0-12-576860-3, google-Books-ID: NFESAQAAIAAJ, 1981.

Renka, R. J.: Algorithm 772: STRIPACK: Delaunay triangulation and Voronoi diagram on the surface of a sphere, ACM Trans. Math. Softw., 23, 416–434, https://doi.org/10.1145/275323.275329, 1997.

Salles, T.: Badlands: A parallel basin and landscape dynamics model, SoftwareX, 5, 195–202, https://doi.org/10.1016/j.softx.2016.08.005, 2016.

Schmeling, H., Babeyko, A. Y., Enns, A., Faccenna, C., Funiciello, F., Gerya, T., Golabek, G. J., Grigull, S., Kaus, B. J. P., Morra, G., Schmalholz, S. M., and van Hunen, J.: A benchmark comparison of spontaneous subduction models—Towards a free surface, Physics of the Earth and Planetary Interiors, 171, 198–223, https://doi.org/10.1016/j.pepi.2008.06.028, 2008.

Simpson, G.: Dynamic interactions between erosion, deposition, and three-dimensional deformation in compressional fold belt settings, J. Geophys. Res., 109, doi:10.1029/2003JF000 111, 2004.

Stern, R. J. and Gerya, T. V.: Chapter 13 - Co-Evolution of Life and Plate Tectonics: The Biogeodynamic Perspective on the Mesoproterozoic-Neoproterozoic Transitions, in: Dynamics of Plate Tectonics and Mantle Convection, edited by Duarte, J. C., pp. 295–319, Elsevier, ISBN 978-0-323-85733-8, https://doi.org/10.1016/B978-0-323-85733-8.00013-5, 2023.

Tackley, P. J.: Effects of strongly temperature-dependent viscosity on time-dependent, three-dimensional models of mantle convection, Geophysical Research Letters, 20, 2187–2190, https://doi.org/10.1029/93GL02317, _eprint: https://onlinelibrary.wiley.com/doi/pdf/10.1029/93GL02317, 1993.

Tackley, P. J.: Modelling compressible mantle convection with large viscosity contrasts in a three-dimensional spherical shell using the yin-yang grid, Physics of the Earth and Planetary Interiors, 171, 7–18, https://doi.org/10.1016/j.pepi.2008.08.005, 2008.

Tackley, P. J. and King, S. D.: Testing the tracer ratio method for modeling active compositional fields in mantle convection simulations, Geochem. Geophys. Geosyst., 4, doi:10.1029/2001GC000 214, 2003.

Tezduyar, T. E.: Interface-tracking and interface-capturing techniques for finite element computation of moving boundaries and interfaces, Computer Methods in Applied Mechanics and Engineering, 195, 2983–3000, https://doi.org/10.1016/j.cma.2004.09.018, 2006.

Tobis, M., Schafer, C., Foster, I., Jacob, R., and Anderson, J.: FOAM: Expanding the Horizons of Climate Modeling, in: SC '97: Proceedings of the 1997 ACM/IEEE Conference on Supercomputing, pp. 27–27, https://doi.org/10.1145/509593.509620, 1997.

Trompert, R. A. and Hansen, U.: The application of a finite-volume multigrid method to 3-dimensional flow problems in a highly viscous fluid with a variable viscosity, Geophys. Astrophys. Fluid Dyn., 83, 261–291, 1996.

Wolf, S. G., Huismans, R. S., and Braun, J.: Tectonics and Surface Processes During Collisional Orogenesis—Exploring the Parameter Space of the Beaumont Number, Journal of Geophysical Research: Solid Earth, 130, https://doi.org/10.1029/2024jb030439, 2025.

Zerkle, A. L.: Biogeodynamics: bridging the gap between surface and deep Earth processes, Philosophical Transactions of the Royal Society A: Mathematical, Physical and Engineering Sciences, 376, 20170 401, https://doi.org/10.1098/rsta.2017.0401, 2018.